

TD-CARMA: Painless, accurate, and scalable estimates of gravitational-lens time delays with flexible CARMA processes

ANTOINE D. MEYER,^{1,2} DAVID A. VAN DYK ¹ HYUNGSUK TAK ^{3,4,5} AND ANETA SIEMIGINOWSKA ²

¹*Statistics Section, Department of Mathematics, Imperial College London, 180 Queen's Gate, London, UK SW7 2AZ*

²*Center for Astrophysics | Harvard & Smithsonian, 60 Garden Street, Cambridge, MA 02138, USA*

³*Department of Statistics, Pennsylvania State University, University Park, PA 16802, USA*

⁴*Department of Astronomy and Astrophysics, Pennsylvania State University, University Park, PA 16802, USA*

⁵*Institute for Computational and Data Sciences, Pennsylvania State University, University Park, PA 16802, USA*

Submitted to The Astrophysical Journal

ABSTRACT

Cosmological parameters encoding our understanding of the expansion history of the Universe can be constrained by the accurate estimation of time delays arising in gravitationally lensed systems. We propose TD-CARMA, a Bayesian method to estimate cosmological time delays by modelling the observed and irregularly sampled light curves as realizations of a Continuous Auto-Regressive Moving Average (CARMA) process. Our model accounts for heteroskedastic measurement errors and microlensing, an additional source of independent extrinsic long-term variability in the source brightness. We obtain a sample from the joint posterior distribution of the model parameters using a nested sampling approach. This allows for “painless” Bayesian Computation, dealing with the expected multi-modality of the posterior distribution in a straightforward manner and not requiring the specification of starting values or an initial guess for the time delay, unlike existing methods. In addition, the proposed sampling procedure automatically evaluates the Bayesian evidence, allowing us to perform principled Bayesian model selection. TD-CARMA is parsimonious, and typically includes no more than a dozen unknown parameters. We apply TD-CARMA to doubly lensed quasars HS 2209+1914, SDSS J1001+5027, SDSS J1206+4332, , estimating their time delays as -21.96 ± 1.448 , 120.93 ± 1.015 , 111.51 ± 1.452 respectively.

Keywords: Astrostatistics technique (1886); Astrostatistics tools (1887); Bayesian statistics (1900); Quasars (1319); Gravitational lensing (670); Nested sampling (1894); Light curves (918); Time series analysis (1916)

1. INTRODUCTION

Cosmological parameters describing the evolution and current state of the Universe through the Λ CDM model, such as the Hubble constant H_0 , are measured by combining baryonic acoustic oscillations measurements and cosmic microwave background observations (Ade et al. 2014). However, cosmological probes are subject to statistical and systematic errors, and individual probes are not able to uniquely constrain the cosmological mod-

els (Rathna Kumar et al. 2013). Combining parameter constraints obtained from different techniques can help break degeneracies associated with specific methods (Tewes et al. 2013). In particular, Refsdal (1964) shows that independent constraints on the cosmological parameters can be derived from the measurement (or estimation) of time delays in quasars subject to strong gravitational lensing by a foreground galaxy. This time delay cosmography (Treu & Marshall 2016; Treu et al. 2022; Birrer et al. 2022) has since become an important cosmological probe, especially in the presence of the Hubble tension (Verde et al. 2019; Shah et al. 2021).

Observations of lensed quasar systems are increasingly available, and the upcoming Vera C. Rubin Observatory is expected to monitor around 1000 strongly lensed quasars (Abell et al. 2009; Dobler et al. 2015). This has prompted the development of numerical and statistical analysis tools for cosmological time delays, notably encouraged by the 2015 Strong Lens Time Delay Challenge (TDC) (Dobler et al. 2015; Liao et al. 2015). The accurate estimation of cosmological time delays has been challenging because of several unusual features in the light curve data. First, celestial cycles and observational patterns cause light curve data to be irregularly sampled and to feature large seasonal gaps. Second, the observed magnitudes of light curves are subject to heteroskedastic measurement errors. Finally, brightness fluctuations in the observed light curves are induced by multiple sources of variability, which all should be taken into account for meaningful modeling and accurate estimation. Indeed, in addition to the intrinsic variability in the source, strong gravitational lensing magnifies the brightness of the light curves, and a microlensing effect may independently encode extrinsic long-term variability in the observed light curves.

Cosmological time delay estimation has been an active research area in astronomy for decades. We refer readers to Linder (2011), Treu & Marshall (2016), Suyu et al. (2017), and Treu et al. (2022) for an overview of time delay cosmography, and to Eulaers et al. (2013a), Tewes et al. (2013), Liao et al. (2015) and Tak et al. (2017) for detailed methodological presentations. See also Courbin et al. (2018), Bonvin et al. (2016, 2018, 2019), and Millon et al. (2020a) for recent advances in time delay estimation methodology.

In a broad sense, time delay estimation techniques can be categorized into non-parametric and parametric methods. Non-parametric time delay estimation methods minimize a measure of difference between the lensed light curves directly from the data and provide uncertainty estimates using Monte Carlo simulations (Pelt et al. 1994). Parametric techniques, on the other hand, model the stochastic variability of AGN light curves within either a Bayesian or a likelihood-based frameworks.

In the non-parametric family of estimation techniques, Aghamousa & Shafieloo (2014) maximize the cross-correlation between smoothed versions of the lensed light curves to estimate the time delay, and produce error estimates through simulations. Similarly, Rathna Kumar et al. (2013) minimize the residuals of a high-pass filtered difference light curve between the lensed quasar light curves. Bag et al. (2022) propose a Gaussian-smoothing based non-parametric method to identify and

measure time delays in lensed quasar images. In the parametric family of techniques, examples include Hogg et al. (2013) who perform Gaussian Process (GP) regression to model the intrinsic light curve and who use a free-knot spline technique. More recently, Bag et al. (2021) developed a Bayesian method to identify gravitationally lensed Type Ia supernovae (SNe Ia) from unresolved light curves and measure their time delays, and Donnan et al. (2021) propose a time delay estimation method based on a running optimal average (ROA) model for the light curve data.

In this paper, we build upon and address limitations of existing Bayesian techniques, using the method developed in Tak et al. (2017) as our main reference. The Bayesian inference paradigm allows us to directly quantify the uncertainty in the time delay parameter. Tak et al. (2017) develop a Bayesian method and apply it to estimate time delays in doubly and quadruply lensed quasar light curves. They model the intrinsic quasar light curve as a realization of a Damped Random Walk (DRW) process (usually referred to as an Ornstein-Uhlenbeck process in the statistical literature) and assume that the light curves are time and magnitude shifted copies of one another. Hereafter we label this method as TD-DRW. Microlensing is also directly accounted for in TD-DRW, and is modeled as a polynomial regression, usually of third order (Kochanek et al. 2006; Courbin et al. 2011; Morgan et al. 2012; Tak et al. 2017). The reader is referred to Tewes et al. (2013) for a review on techniques designed to handle extrinsic variability due to microlensing in time delay estimation problems.

The TD-DRW method performed well in the TDC (Liao et al. 2015), perhaps in part because the TDC data had been generated under a DRW process. The aim of this paper is to further develop this method in order to improve the accuracy of time delay estimation, by refining the intrinsic quasar light curve model and addressing several additional limitations.

Following the introduction of the DRW process as a modeling tool for the stochastic variability in AGN light curves by Kelly et al. (2009), numerous empirical studies have supported its use or astronomical time-series data analysis (MacLeod et al. 2010; Kozłowski et al. 2009; Kim et al. 2012; Andrae et al. 2013). However, the inflexibility of DRW (which only incorporates two free parameters) has limited its broader use (Mushotzky et al. 2011; Zu et al. 2013; Graham et al. 2014; Kasliwal et al. 2015; Kozłowski 2016, 2017), and has motivated the adoption of more general models. Specifically, Kelly et al. (2014) introduced Continuous Autoregressive Moving Average (CARMA) processes as a

flexible tool for characterizing AGN variability. Recent astrophysical studies (Kasliwal et al. 2017; Moreno et al. 2019; Ryan et al. 2019; Stone et al. 2022) have empirically shown that the CARMA process can successfully model various types of stochastic variability in AGN light curves.

Indeed, the Power Spectrum Density (PSD) of a CARMA process can account for multiple break-like features and quasi-periodic oscillations (QPOs) in their PSDs, which are characteristics typically observed in AGN data (Kelly et al. 2014; Kasliwal et al. 2017; Ryan et al. 2019). As explained in Liao et al. (2015), AGNs and particularly quasars are sources for which strong gravitational lensing is more likely to happen, since they are very distant from Earth (thus increasing the likelihood that a candidate lens stands between the source and Earth) and very luminous. Therefore, we update the TD-DRW method introduced in Tak et al. (2017) by generalizing the intrinsic light curve model from a DRW process to CARMA processes, and hereafter refer to our method as TD-CARMA.

In addition to leveraging CARMA processes to perform a finer modeling of the intrinsic light curve, we address computational limitations of existing time delay estimation methods. For example, Kelly et al. (2014) report that the likelihood function (and thus the resulting joint posterior distribution) of the CARMA model may contain multiple local maxima, especially when the degree of the auto-regression component is greater than one. It is also well known that time delay estimates under the TD-DRW may suffer from multi-modality (Tak et al. 2017, 2018). Because it combines two sources of multi-modality, namely a CARMA model and time delay, it is not unexpected that TD-CARMA exhibits more severe multi-modality in its posterior distribution.

To address this, we perform Bayesian parameter inference using nested sampling (Skilling 2006) instead of the Markov chain Monte Carlo (MCMC) methods used by Kelly et al. (2014) and Tak et al. (2018). Specifically, we use the pyMultiNest (Buchner 2016) python implementation of the multi-modal ellipsoidal nested sampling algorithm developed by Feroz et al. (2009), known as MultiNest.

MultiNest has two important computational advantages over MCMC in this setting. First, most time delay estimation methods require and are highly sensitive to an initial guess for the time delay parameter. For instance, in TD-DRW, Tak et al. (2017) compute the prohibitively expensive profile likelihood of the time delay parameter to find a starting value for their MCMC algorithm, and all methods described in Tewes et al. (2013) must be initialized near a plausible value of the time de-

lay. Unlike MCMC, however, nested sampling methods do not evolve a single path through the parameter space and thus do not require the input of an initial value for the model parameters. This means TD-CARMA only requires the specification of a range of possible values for each of the parameters. Also, MultiNest computes the Bayesian evidence of the fitted model simultaneously to the posterior sampling, which solves the model selection problem of choosing the auto-regressive and moving average orders of the CARMA process, as well as the degree of the polynomial regression used to model microlensing, without any further computation.

The improvements that TD-CARMA offers over existing methods introduced in Tewes et al. (2013), Liao et al. (2015) and Tak et al. (2017) can be summarized as follows:

1. *Flexibility and Accuracy.* TD-CARMA leverages flexible CARMA processes which are well suited to model a wide range of AGN light curves. In addition, this work shows that these flexible models can also improve the accuracy of time delay estimates.
2. *Painless Bayesian Computation.* Using MultiNest for Bayesian computation means that TD-CARMA does not require a plausible initial value for the time delay parameter. MultiNest also allows us to tackle the severe multi-modality in the joint posterior distribution of the TD-CARMA model parameters.
3. *Scalability.* The model likelihood is efficiently computed with linear complexity $O(n)$. This makes TD-CARMA scalable to large datasets.
4. *Built-in Model Selection.* The proposed MultiNest fit automatically evaluates the Bayesian evidence of the fitted models and allows us to perform principled Bayesian model comparison and selection without any additional computation.
5. *Parsimony.* Some methods featured in Liao et al. (2015) and Tewes et al. (2013) incorporate hundreds of parameters, and sometimes have parameter spaces that scale with the data. In contrast, in our numerical studies the number of unknown model parameters used by TD-CARMA ranges from 6 to 15. Parsimonious methods are easier to interpret scientifically and also statistically, since better behaved likelihoods produce more Gaussian estimators, and more easily quantifiable errors.

The rest of the paper is organized as follows. Section 2 presents the time delay estimation method TD-

Table 1. Glossary of notation used in this work.

Data	
Symbol	Description
t	Observation times
x	Brightness measurements for light curve A
y	Brightness measurements for light curve B
z	Composite light curve
δ^x	Standard deviations for light curve A
δ^y	Standard deviations for light curve B
Model Parameters	
Symbol	Description
Δ	Time delay (days)
θ	Microlensing polynomial regression coefficients
α	CARMA auto-regressive coefficients
β	CARMA moving average coefficients
τ	DRW mean-reversion timescale
σ^2	CARMA and DRW white noise variance
μ	CARMA and DRW long-term mean
Ω	Full set of either DRW or CARMA parameters
Model Hyperparameters ^a	
Symbol	Description
p	Auto-regressive order
q	Moving average order
m	Microlensing polynomial regression order
Other Symbols	
Symbol	Description
\mathcal{Z}	Bayesian evidence
\mathcal{Z}_i	Bayesian evidence for Model i or Mode i
π_i	Relative probability of Model i or Mode i
ϕ	Generic parameter vector
Φ	Range of possible values for generic parameter ϕ

^a The hyperparameters index competing models. Values for the hyperparameters are selected via the Bayesian evidence or the relative probabilities of the models considered; see Section 3.1.

CARMA. Section 3 details our Bayesian inferential procedure, including MultiNest. In Section 4, we show through simulation studies that the CARMA-based time delay estimation method is more applicable and accurate than several popular methods. In Section 5, we apply the method to doubly lensed quasars HS 2209+1914, SDSS J1001+5027, SDSS J1206+4332. Finally, Section 6 presents further research directions and concludes. Background material and detailed results from our numerical studies appear in a number of appendices.

2. A CARMA-BASED TIME DELAY MODEL

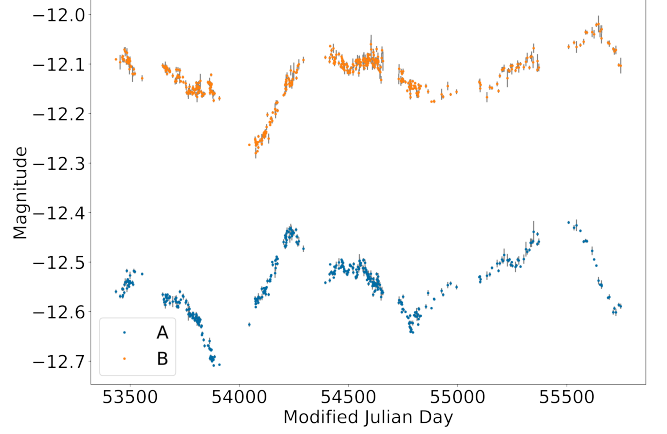


Figure 1. Data for doubly lensed quasar SDSS J1001+5027 Kumar et al. (2013), studied in Section 5.3 of this work.

Strong gravitational lensing can produce multiple copies of the observed source’s light curve. While our statistical model is explicitly designed for the doubly lensed case, it can be applied pairwise to more complex systems (as in Tak et al. 2017) and could be generalised to the quadruply lensed case in order to account for correlations among the time delay parameters. Henceforth, however, we consider the doubly lensed case.

2.1. Data

The data for a doubly lensed quasar observed for n epochs can be written as $\mathbf{D} = \{t_i, x_i, \delta_i^x, y_i, \delta_i^y\}_{i=1}^n$, where t_i denotes the measurement time (in days) of observation epoch i , x_i and y_i denote the observed brightness of the light curves of the two lensed images of the same quasar at time t_i (typically measured in apparent magnitude), and δ_i^x and δ_i^y denote the standard deviation of the measurement error on x_i and y_i (thus encoding the heteroskedasticity of measurement errors). Table 1 summarizes the symbols used in this work. Figure 1 shows the data for doubly lensed quasar SDSS J1001+5027, where light curve B is delayed from light curve A, for $\Delta \approx 119.3$ days according to previous analyses (a figure reproduced from Kumar et al. 2013).

2.2. Time Delay Estimation Framework

The general idea of our time delay estimation framework is to reconstruct the common intrinsic quasar light curve from the measurements of its two lensed counterparts, under the assumption that they are time and magnitude shifted versions of one another, up to a microlensing term, where the time shift corresponds to the time delay Δ .

The magnitude measurements $\mathbf{x} = \{x_i\}_{i=1}^n$ and $\mathbf{y} = \{y_i\}_{i=1}^n$ are assumed to be discrete realizations of unobserved continuous light curves $X(t)$ and $Y(t)$, which

represent the true source magnitudes at time $t \in \mathbb{R}$. As a result of the strong gravitational lensing phenomenon, we assume that $Y(t)$ is a time shifted version of $X(t)$, which yields

$$Y(t) = X(t - \Delta), \quad (1)$$

where Δ is the time delay in days. In addition to the intrinsic brightness fluctuations of the source, two lensing effects induce extra variability in the observed magnitudes. First, strong gravitational lensing magnifies the brightness of each light curve to different degrees. Therefore \mathbf{x} and \mathbf{y} can exhibit different average magnitudes. Tak et al. (2017) take this effect into account by introducing an intercept term θ_0 as follows:

$$Y(t) = X(t - \Delta) + \theta_0. \quad (2)$$

Second, additional extrinsic long-term variability might be caused by microlensing, a lensing effect occurring when a light ray passes close to a moving object near the lensing galaxy. This effect is typically modeled by a polynomial regression of order m on time (Kochanek et al. 2006; Courbin et al. 2011; Morgan et al. 2012; Tak et al. 2017). That is,

$$Y(t) = X(t - \Delta) + \mathbf{w}_m(t - \Delta)\boldsymbol{\theta}, \quad (3)$$

where $\mathbf{w}_m(t - \Delta) = \{1, t - \Delta, \dots, (t - \Delta)^m\}$ is the vector containing the polynomial time variables, and $\boldsymbol{\theta} = \{\theta_0, \dots, \theta_m\}$ is the microlensing (regression) coefficients. We treat m as a hyperparameter. That is, it indexes the choice of model and its value is set by comparing several values as part of statistical model selection, see Section 3.1.

Given the parameters Δ and $\boldsymbol{\theta}$, we can construct a composite light curve that combines two lensed light curves (as if they were a single light curve) by adjusting one light curve according to the model in (3). The combined observation times are composed of the original observation times and the time-delay-shifted observation times, $\mathbf{t}^\Delta = \{t_i\}_{i=1}^n \cup \{t_i - \Delta\}_{i=1}^n$. We denote the magnitudes of the composite light curve by $\mathbf{z} = \{z_j\}_{j=1}^{2n}$, where each z_j is defined as

$$z_j = \begin{cases} x_i & \text{for some } i \text{ if } t_j^\Delta \text{ is in } \mathbf{t}, \\ y_i - \mathbf{w}_m(t_j - \Delta)\boldsymbol{\theta} & \text{for some } i \text{ if } t_j^\Delta \text{ is in } \mathbf{t} - \Delta. \end{cases} \quad (4)$$

We can similarly define the vector of measurement error standard deviations as $\boldsymbol{\delta}^z = \{\delta_i^z\}_{i=1}^{2n}$ with:

$$\delta_j^z = \begin{cases} \delta_i^x & \text{for some } i \text{ if } t_j^\Delta \text{ is in } \mathbf{t}, \\ \delta_i^y & \text{for some } i \text{ if } t_j^\Delta \text{ is in } \mathbf{t} - \Delta. \end{cases} \quad (5)$$

We assume that the vector of measurements for the composite light curve \mathbf{z} is the discrete realization of an unobserved continuous-time light curve $Z(t)$, which represents the true source magnitude of the AGN at time $t \in \mathbb{R}$. Therefore, given Δ and $\boldsymbol{\theta}$, we only need to model the stochastic variability of the single latent light curve $Z(t)$. The DRW and CARMA processes have been widely used to model the stochastic nature of the intrinsic variability in AGN light curves since Kelly et al. (2009, 2014) introduced them to the astronomical community.

2.3. DRW and CARMA Processes

The DRW process has already been integrated into time delay estimation methodology by Tak et al. (2017), and we propose an extension of this method by modelling the intrinsic light curve $Z(t)$ with the more general CARMA processes.

The Damped Random Walk (DRW) process is defined as the solution of the stochastic differential equation:

$$dZ(t) = -\frac{1}{\tau}(Z(t) - \mu)dt + \epsilon(t), \quad (6)$$

where μ is the long-term mean of the process, τ is the timescale for the process to revert to its long-term mean and $\epsilon(t)$ is a white noise process with variance σ^2 (that is, $\epsilon(t) \sim N(0, \sigma^2)$) governing the stochastic fluctuations in the process (Brockwell & Davis 2002).

A CARMA process is indexed by two hyperparameters: its auto-regressive order p and moving average order q . The process is denoted CARMA(p, q) and is defined as the solution of the stochastic differential equation:

$$\begin{aligned} \frac{d^p Z(t)}{dt^p} + \alpha_{p-1} \frac{d^{p-1} Z(t)}{dt^{p-1}} + \dots + \alpha_0 Z(t) = \\ \mu dt + \beta_q \frac{d^q \epsilon(t)}{dt^q} + \beta_{q-1} \frac{d^{q-1} \epsilon(t)}{dt^{q-1}} + \dots + \epsilon(t), \end{aligned} \quad (7)$$

where $\boldsymbol{\alpha} = \{\alpha_0, \dots, \alpha_{p-1}\}$ are the auto-regressive parameters, $\boldsymbol{\beta} = \{\beta_1, \dots, \beta_q\}$ are the moving average coefficients and $\epsilon(t)$ is a white noise process with variance σ^2 . We also define $\alpha_p = 1$ and $\beta_0 = 1$, and note that the DRW is equivalent the CARMA(1,0) process with $\tau = 1/\alpha_0$.

DRW has a limited applicability in describing the stochastic variability in AGN light curves, since for instance it cannot account for quasi-periodic variability features and multiple auto-correlation timescales. CARMA processes, however, can account for such features and are thus suitable to characterize the variability in a wide range of AGN light curves. The reader is referred to Appendix A, Kelly et al. (2009) and Kelly et al. (2014) for technical reviews of the mathematics governing the dynamics of the DRW and CARMA processes.

2.4. Time Delay Model Likelihood

DRW and CARMA processes that are stochastically driven by white noise processes are Gaussian (Kelly et al. 2009, 2014)¹ and their likelihood functions can be evaluated via a Gaussian Process (GP). Let Ω be the parameter vector for the intrinsic light curve $Z(t)$, i.e. $\Omega = (\mu, \sigma^2, \tau)$ for DRW and $\Omega = (\mu, \sigma^2, \alpha, \beta)$ for CARMA. , we can write the likelihood function of the model parameters given observed data as:

3. BAYESIAN INFERENCE AND STATISTICAL COMPUTATION

3.1. Bayesian Inference and Model Selection

We adopt a Bayesian statistical approach to perform parameter inference, which allows us to quantify uncertainty in the model parameters, including Δ , via their joint posterior distribution, given the observed data. From this we can compute point estimates and error bars, as required. Once the prior distributions are specified and the data are observed (and incorporated into the model via the likelihood function), Bayes' Theorem gives the expression for the posterior distribution of the parameters, i.e., the updated summary of information about the model parameters after observing the data:

$$p(\Delta, \theta, \Omega | \mathbf{D}) = \frac{L(\Delta, \theta, \Omega | \mathbf{D}) p(\Delta, \theta, \Omega)}{p(\mathbf{D})}, \quad (8)$$

where $L(\Delta, \theta, \Omega | \mathbf{D})$ is the likelihood under the model defined in Equation ?? and is equal to $p(\mathbf{D} | \Delta, \theta, \Omega)$, the sampling distribution of the data given the model parameters, $p(\Delta, \theta, \Omega)$ is the prior distribution of the parameters, and $p(\mathbf{D})$ is the marginal distribution of the data, otherwise known as the Bayesian evidence. The Bayesian evidence, hereafter denoted by \mathcal{Z} , i.e., $\mathcal{Z} = p(\mathbf{D})$, can be used for model comparisons, and is defined as:

$$\mathcal{Z} = \int_{\Phi} p(\mathbf{D} | \phi) p(\phi) d\phi, \quad (9)$$

where ϕ is a generic (vector) parameter and Φ is the (multivariate) set of possible values for ϕ . The Bayesian evidence \mathcal{Z} is a measure of the “goodness of fit” of a model to the data \mathbf{D} , so that models with higher evidence provide a better explanation of the data. The definition of \mathcal{Z} naturally incorporates Occam's razor, as more complex models, i.e., models defined on higher-dimensional parameter spaces, are penalized if they do not sufficiently improve the fit to the data (Jefferys & Berger 1991).

Suppose we fit each of several models, M_1, \dots, M_K and wish to identify the models that dominate in terms of their evidence. For example, we may wish to compare TD-DRW(m) and TD-CARMA(p, q, m) for each of several combinations of values of the hyperparameters, p , q , and m (auto-regressive, moving average and microlensing orders).

For this, it is useful to compute the relative probability of each considered model,

$$p(M_i) = \frac{\mathcal{Z}_i}{\sum_{k=1}^K \mathcal{Z}_k}. \quad (10)$$

In TD-CARMA we must specify the hyperparameter triplet (p, q, m) that best fits the data. Statistically, this is a model selection problem. Because CARMA(p, q) models are non-nested, likelihood ratio tests cannot be used for model selection (Protassov et al. 2002; Kelly et al. 2014). In the astrophysics literature, when fitting CARMA processes to light curve data, (p, q) pairs are selected using information criteria such as AIC (Kelly et al. 2014) or DIC (Kasliwal et al. 2017). These may require additional computation (e.g., AIC requires the computation of the Maximum Likelihood Estimator) and rely on asymptotic approximations. We instead use the principled Bayesian evidence, \mathcal{Z} , which is a commonly used model selection approach in the Bayesian regime (mostly via Bayes factors, e.g., Kass & Raftery 1995). The Bayesian evidence is conveniently computed directly by MultiNest² at the same time it generates a posterior sample, see Section 3.3.

3.2. Prior Distributions

We assume uniform prior distributions for each model parameter. Specifically, we set a uniform prior for the time delay Δ on the range $[t_1 - t_n, t_n - t_1]$. In instances where it is clear which light curve is delayed, the prior distribution for Δ can accordingly be reduced to $[t_1 - t_n, 0]$ or $[0, t_n - t_1]$. The prior for the microlensing parameters, θ , is defined to be uniform on the range $[-10^5, 10^5]$. The average apparent magnitude μ is given a uniform prior on the range $[-30, 30]$, which covers a magnitude range from that of the Sun to that of the faintest object observable by the Hubble Space Telescope (Tak et al. 2017). The other TD-CARMA parameters α , β and σ are sampled on the logarithmic scale, with priors on their (natural) logs defined to be

¹ CARMA processes can be defined as stochastically driven by non-Gaussian Levy processes, in which case they are not Gaussian (Brockwell 2001).

² MultiNest returns the logarithm of the Bayesian evidence, i.e., $\ln(\mathcal{Z}_i)$.

uniform on the range $[-15, 15]$. This largely covers the range of frequencies probed by the data³.

3.3. Multiple Modes and MultiNest

We obtain a sample from the posterior distribution $p(\Delta, \beta, \Omega | \mathbf{D})$ in Equation (8) via the MultiNest implementation of (multi-modal ellipsoidal) nested sampling (Feroz et al. 2009; Buchner 2016), for both TD-DRW and TD-CARMA. In the case of time delay estimation, inference via nested sampling has a variety of advantages over traditional MCMC methods, including the computation of the Bayesian evidence to perform model selection (see Section 3.1), and the efficient sampling of multi-modal posterior distributions.

The multi-modality in this problem is complicated, because it manifests itself in two distinct ways.

First, the posterior distribution of CARMA(p, q) parameters is notoriously multi-modal, when $p > 1$ (Kelly et al. 2014). Moreover, even for fixed p and q there is potential multi-modality in the time delay parameters Δ and θ (e.g., Tak et al. 2017).

Sampling procedures in Tak et al. (2017) have difficulties navigating such posteriors even with the simpler TD-DRW model. Thus, we use MultiNest, which is specifically designed to efficiently sample from complicated and multi-modal posterior distributions. MultiNest identifies the multiple modes in the posterior, partitions the parameter space into regions on which the separated modes are supported, and evaluates the local evidence of each identified mode.

Specifically, assuming MultiNest identifies Mode i defined on a region Φ_i of the parameter space Φ , the local evidence \mathcal{Z}_i of Mode i is defined as:

$$\mathcal{Z}_i = \int_{\Phi_i} p(\mathbf{D}|\phi)p(\phi)d\phi. \quad (11)$$

The local evidence \mathcal{Z}_i can be used to compute the relative probability of Mode i , denoted as π_i and defined as:

$$\pi_i = \int_{\Phi_i} p(\phi|\mathbf{D})d\phi = \frac{1}{\mathcal{Z}} \int_{\Phi_i} p(\mathbf{D}|\phi)p(\phi)d\phi = \frac{\mathcal{Z}_i}{\mathcal{Z}}.$$

where \mathcal{Z} is the (total) Bayesian evidence.

In the event of a multi-modal posterior distribution, computing the above quantities offers a principled way of quantifying the relative probability of the several modes.

3.4. Constraints and Parametrizations

³ The maximum and minimum frequencies probed by the data are defined as $1/\min(\Delta t)$ and $1 / (\max(t) - \min(t))$ where $\Delta t := \{t_{i+1} - t_i\}_{i=1}^{2n-1}$

As discussed in Section A.2, we use an alternative parametrization of the auto-regressive polynomial $A(z)$ to enforce stationarity when fitting CARMA processes. Instead of sampling the auto-regressive parameters α , we sample the coefficients $\mathbf{a} = \{a_1, \dots, a_p\}$ (defined in Section A.2), on the natural log-scale to enforce non-negativity (for stationarity of the resulting CARMA process).

The likelihood of a CARMA process is invariant to permutations in the indices of the roots of the auto-regressive polynomial. In order to avoid identifiability issues, Kelly et al. (2014) imposes ordering constraints on the auto-regressive roots. This, however, involves rejecting Monte Carlo draws that do not satisfy the ordering constraint, which renders sampling inefficient. Since swaps in the indices of the auto-regressive roots that give the same likelihood create mirror modes in the posterior distribution, we do not impose an ordering constraint but rather combine the modes and consider the full posterior in our analyses.

Finally, the polynomial regression coefficients $\theta = \{\theta_1, \dots, \theta_m\}$ are highly correlated in their posterior distribution, since the regression covariates $\{1, t - \Delta, (t - \Delta)^2, \dots, (t - \Delta)^m\}$ are themselves highly correlated. This yields a posterior distribution with complex geometry that is difficult to sample from efficiently. To circumvent this issue, we perform a QR decomposition⁴ (e.g., Gander 1980) of the polynomial regression covariate matrix, a common computational trick in standard regression problems used to de-correlate covariates.

At each iteration, MultiNest proposes new values of the parameters by sampling from their joint prior distribution, constrained to regions of the parameter space corresponding to iso-contours in the likelihood (Feroz et al. 2009). The resolution at which the parameter space is explored therefore depends (at least initially) on the number of points sampled from the prior at each iteration, denoted N_{live} (Feroz et al. 2009), and the range covered by the prior. We repeatedly fitted our models with different values of N_{live} , and found that $N_{\text{live}} = 400$ for our simulations and $N_{\text{live}} = 1000$ for our dataset applications yield stable results.

3.5. Frequencies in the Fit

⁴ The name ‘‘QR decomposition’’ refers to the notation used in the standard representation of the decomposition, where Q is an orthogonal matrix and R is an upper triangular matrix. We refer readers to the Stan User’s Guide: <https://mc-stan.org/docs/2.29/stan-users-guide/QR-reparameterization.html> for a complete description of the QR decomposition and its use in de-correlating coefficients in linear statistical models.

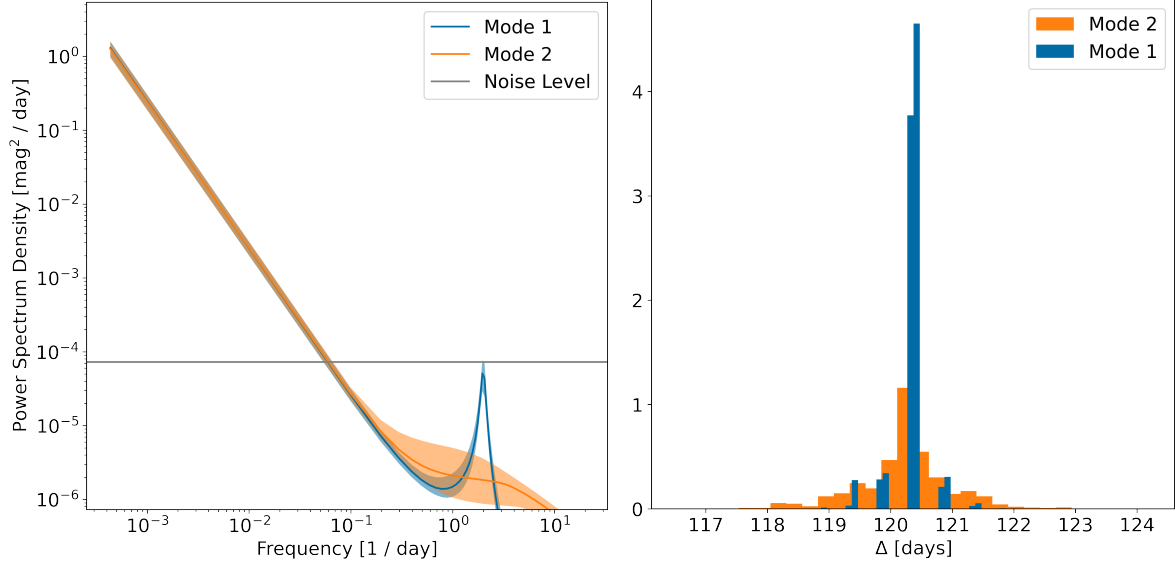


Figure 2. (Left) A Monte Carlo sample from the posterior distribution for the PSD of the intrinsic light curve for quasar SDSS J1001+5027 under TD-CARMA(3, 1, 3). The posterior distribution for the CARMA parameters α, β, σ is bi-modal, with one mode corresponding to a PSD with a frequency around 2 days (Mode 1), and the other without a frequency. The frequency in Mode 1 is below the measurement noise level. (Right) Histogram of posterior draws for Δ , for each of the two modes in the joint posterior distribution computed with TD-CARMA(3, 1, 3), for the SDSS J1001+5027 data. For Mode 1, since a frequency of 2 (day^{-1}) is detected, this constrains Δ to values that are multiple of 0.5 days, and thus drastically reduces the uncertainty. The standard deviation of the posterior of Δ in Mode 2 is 0.686 days, and is 0.224 days in Mode 1.

In the event of a multi-modal posterior distribution of the CARMA(p, q) model parameters, $\Omega = \{\alpha, \beta, \sigma\}$, one or more of the modes might correspond to a frequency in the posterior PSD (i.e., the PSD features a Lorentzian centered away from 0). For example, the left panel of Figure 2 shows a bi-modal PSD, where Mode 1 detects a frequency at ≈ 2 days. This posterior PSD was obtained by fitting TD-CARMA(3,1,3) to a doubly lensed quasar dataset SDSS J1001+5027, the full analysis of which appears in Section 5.3.

Following Kelly et al. (2014), we can attribute a detected frequency in the inferred PSD of the intrinsic light curve to either the signal or the noise by comparing the posterior distribution of the power for the detected frequency with the measurement noise level⁵. If the posterior distribution of power for the detected frequency is supported above the measurement noise level, we recognize the frequency as a feature of the light curve. Otherwise, this provides statistical evidence that the CARMA processes are essentially identifying a periodic artifact of the noise.

If a detected frequency were to be attributed to the intrinsic light curve, it would dramatically reduce the

size of the error bars for the estimate of Δ , as shown in the right panel of Figure 2 (and Tables 12, 14 and 15 in Appendix B). Indeed, when a frequency is detected in the PSD for the intrinsic light curve, this naturally constrains Δ to multiples of the frequency. Thus, TD-CARMA can leverage a frequency that is not attributed to the noise to dramatically reduce the error bars on Δ . This would not be possible with TD-DRW, for instance.

4. SIMULATED DATA ANALYSES

In this Section, we generate synthetic data and study the prediction accuracy and coverage probability of the estimates and credible intervals obtained for Δ with TD-CARMA.

We simulate doubly lensed synthetic datasets under nine different data generation models. The nine models were specified by three different continuous time series processes: DRW (i.e., CARMA(1,0)), CARMA(2,1) and CARMA(3,1). For each of the nine resulting data generating processes for the microlensed light curves, replicate datasets are simulated, sharing all model parameters Ω related to the latent process. This yields datasets in total. In the next few paragraphs, we detail our procedure for the simulation of the synthetic data sets which, in an effort to mimic potential light curves from the Rubin Observatory Legacy Survey of Space and

⁵ The measurement noise level is computed as $2\bar{\Delta}_t\bar{\delta}^2$ where $\bar{\Delta}_t$ is the average time difference between consecutive time measurements, and $\bar{\delta}^2$ is the average measurement error variance.

Table 2.

Metric	Data Generation Model									Average
	DRW(1)	DRW(2)	DRW(3)	C(2,1,1)	C(2,1,2)	C(2,1,3)	C(3,1,1)	C(3,1,2)	C(3,1,3)	
Bias	-0.00643	-0.00437	-0.00812	-0.01099	-0.01144	-0.01618	-0.00223	0.00026	0.01877	0.00452
Variance	0.00589	0.00622	0.00496	0.00164	0.00187	0.00250	0.00212	0.00208	0.03592	0.00702
RMSE	0.00593	0.00624	0.00503	0.00176	0.00201	0.00277	0.00213	0.00208	0.03628	0.00713
Accuracy	-0.00022	-0.00015	-0.00028	-0.00038	-0.00040	-0.00056	-0.00008	0.00001	0.00065	-0.00016
Precision	0.00321	0.00335	0.00312	0.00182	0.00178	0.00168	0.00543	0.00596	0.00594	0.00358
Chi-Squared	0.63669	0.64569	0.63379	0.63285	0.72019	0.94437	0.09517	0.06484	1.24116	0.62386
1σ Coverage ^a	0.77	0.78	0.76	0.76	0.72	0.56	0.99	0.99	0.71	0.78
2σ Coverage ^b	0.99	0.98	0.93	0.99	0.97	0.84	1.0	1.0	0.89	0.96

^aThe theoretical coverage of 1σ intervals is 66%.

^bThe theoretical coverage of 1σ intervals is 95%.

Time⁶, roughly follows the simulation design presented in Liao et al. (2015).

generate the time series parameters Ω for the three different intrinsic light curve models DRW, CARMA(2,1) and CARMA(3,1). When the intrinsic light curve is generated under a DRW process, we set timescale τ to 1000 days. For the CARMA(2,1), we choose α such that the ACF of the process features an exponentially damped sinusoid with a frequency equal to 1/100 days and e -folding time scale of 1/500 days. For the CARMA(3,1) process, we modify the α generated for the CARMA(2,1) process to add an exponential decay with e -folding time scale of 1/1000 days to the ACF of the CARMA(2,1) process⁷. The moving average parameter vector β is sampled uniformly from its prior, defined in Section 3.2. Finally, the σ^2 parameter is computed such that all three intrinsic light curves share the same marginal variance, $R(0)$; expressions for $R(0)$ are given in Equations A1 and A5 in Section A.2. We sample this shared value of $R(0)$ uniformly from the $[0, 10]$ range. Figure 7 shows the ACFs (defined in Sections A.1 and A.2) for the three intrinsic light curve models resulting from this procedure.

Given the generative values of the parameters Ω , Δ , and θ , we create a doubly lensed synthetic dataset as follows.

1. Given Ω , generate an observation of the intrinsic light curve $Z(t)$ at a high-resolution grid of measurement times, with 100,000 evenly spaced epochs over a 1000-day period.

2. Given the values of Δ and θ , generate the high-resolution observations of the light curves $X(t)$ and $Y(t)$, via Equation 3.
3. Down-sample the data to five observational seasons of length four months, and to a median observation cadence of three days. This yields approximately 200 data points for each light curve. The seasonal thinning is the same across all dataset replicates, but the daily thinning is random.
4. Generate measurement error standard deviations $\{\delta_i^x\}_{i=1}^n$ and $\{\delta_i^y\}_{i=1}^n$, sampled from a normal distribution with mean and standard deviation equal to $10\%\sqrt{R(0)}$. The measurements $\{x_i\}_{i=1}^n$ and $\{y_i\}_{i=1}^n$ are then polluted with noise, sampled at each observation time from the normal distributions $N(0, \delta_i^{x^2})$ and $N(0, \delta_i^{y^2})$.

For every generated dataset, we fit different time delay models: TD-DRW, TD-CARMA(2,1) and TD-CARMA(3,1), with $m = \{1, 2, 3\}$.

4.1.

To ensure that our error bars are well-calibrated, we examine the frequency coverage of the posterior intervals.

Figure 3 plots the theoretical coverage against the actual coverage probability observed in our simulation study, for $p_n \in [0, 1]$.

5. ANALYSIS OF LENSED QUASARS FROM COSMOGRAIL

5.1. Overview of Numerical Analysis

In this section, we apply TD-CARMA to a selection of doubly lensed quasar datasets, and compare the resulting estimates to those obtained in the literature. We

⁶ <https://www.lsst.org/about>

⁷ The reader is referred to Kelly et al. (2014) for a description of the transformation from PSD frequencies and time scales to CARMA parameters α .

Table 3. Summary of our analysis (carried out in Section 5, of six doubly lensed quasars from the Sloan Digital Sky Survey (SDSS), observed and previously analysed by the COSMOGRAIL collaboration.

Dataset	COSMOGRAIL reference	COSMOGRAIL estimate	TD-CARMA
SDSS HS2209+1914	Eulaers et al. (2013b)	-20 ± 5	-21.96 ± 1.448
SDSS J1001+5028	Kumar et al. (2013)	119.1 ± 3.3	120.93 ± 1.015
SDSS J1206+4332	Millon et al. (2020b)	113.0 ± 3	111.51 ± 1.452
SDSS J1515+1511	Millon et al. (2020b)	$210.5^{+5.5}_{-5.7}$	210.80 ± 2.18
SDSS J1455+1447	Millon et al. (2020b)	$47.2^{+7.5}_{-7.8}$	45.36 ± 1.93
SDSS J1349+1227	Millon et al. (2020b)	*	432.05 ± 1.950

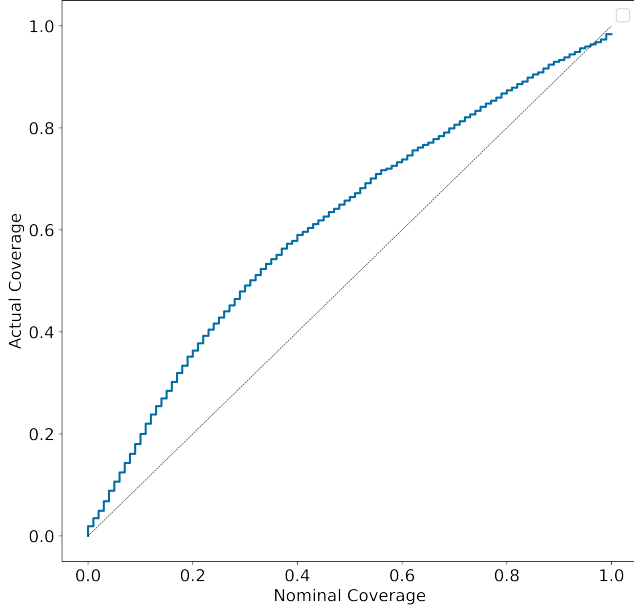


Figure 3. Nominal and actual coverage of generative value of Δ by posterior intervals produced by TD-DRW, TD-CARMA(2,1), and TD-CARMA(3,1) in Simulation Study of Section 4, averaged over the three generative models. The dotted grey line is the line where actual coverage equals theoretical coverage.

have selected quasars that appear to have particularly complex intrinsic light curves and on which TD-DRW failed to return reliable estimates of Δ (using the *timedelay* package of [Tak et al. \(2017\)](#)). Thus, a DRW process may not be sufficiently robust to model the underlying light curves.

For each dataset we fit a total of models. Specifically, we fit TD-DRW with $m = 3$ and TD-CARMA with auto-regressive order $p = \{2, 3, 4\}$, moving average order $q = \{1, 2, 3\}$ and microlensing order $m = \{1, 2, 3\}$, such that $p > q$. In Appendix B, we report the full results of our analyses in tables that give summary statistics for the posterior distribution of the model parameters for each fitted model, including the posterior mean and variance for Δ , the Bayesian (log) evidence for the model, and the posterior mean of the frequency (computed from

the posterior mean of the auto-regressive parameters α) if the inferred PSD features a frequency (or frequencies). In the event of a multi-modal posterior distribution, we report these statistics for each mode and give the value for their Bayesian local (log) evidence, i.e., the mode-specific evidence⁸.

In all cases where the inferred PSD featured a frequency, the associated posterior distribution for the power of the frequency was below the measurement noise level. Therefore, following Section 3.5, we ignore all fits that included a frequency. We elaborate the numerical results for the frequencies analyses for all six examples in Section 5.5.

We select the model with highest Bayesian evidence (or relative probability), and compare its estimates for Δ with those derived by a *baseline model*, specifically our simplest model, TD-CARMA(2,1,3)⁹, and those obtained by other methods in the literature.

5.2. Application I: HS 2209+1914

HS 2209+1914 is a doubly lensed quasar observed as part of the COSMOGRAIL study ([Eulaers et al. 2013b](#)) with four telescopes: Euler, Mercator, Maidanak and HCT, during a total of 8.5 years (2004 to mid 2012). [Eulaers et al. \(2013b\)](#) propose a time delay measurement of $\Delta = -20 \pm 5$ days (using a combination of four different techniques, referenced in Table 5), warning that the lack of obvious fast variability features in the observed light curves and the possible presence of microlensing made it a particularly difficult observation to study.

Our analysis also suggests the presence of a strong microlensing effect in this observation, as indicated by the dependence of the estimated time delay, $\hat{\Delta}$, on the microlensing order m . TD-CARMA models with $m = \{1, 2\}$ microlensing produce estimates of Δ around -40 days, whereas those with $m = 3$ produce $\hat{\Delta} \approx -22$

⁸

⁹ We choose $m = 3$ for our baseline model to ensure that it is sufficiently flexible to capture the potential effect of microlensing. [Moreno et al. \(2019\)](#) notably supported the choice of CARMA(2,1) to model AGN light curves.

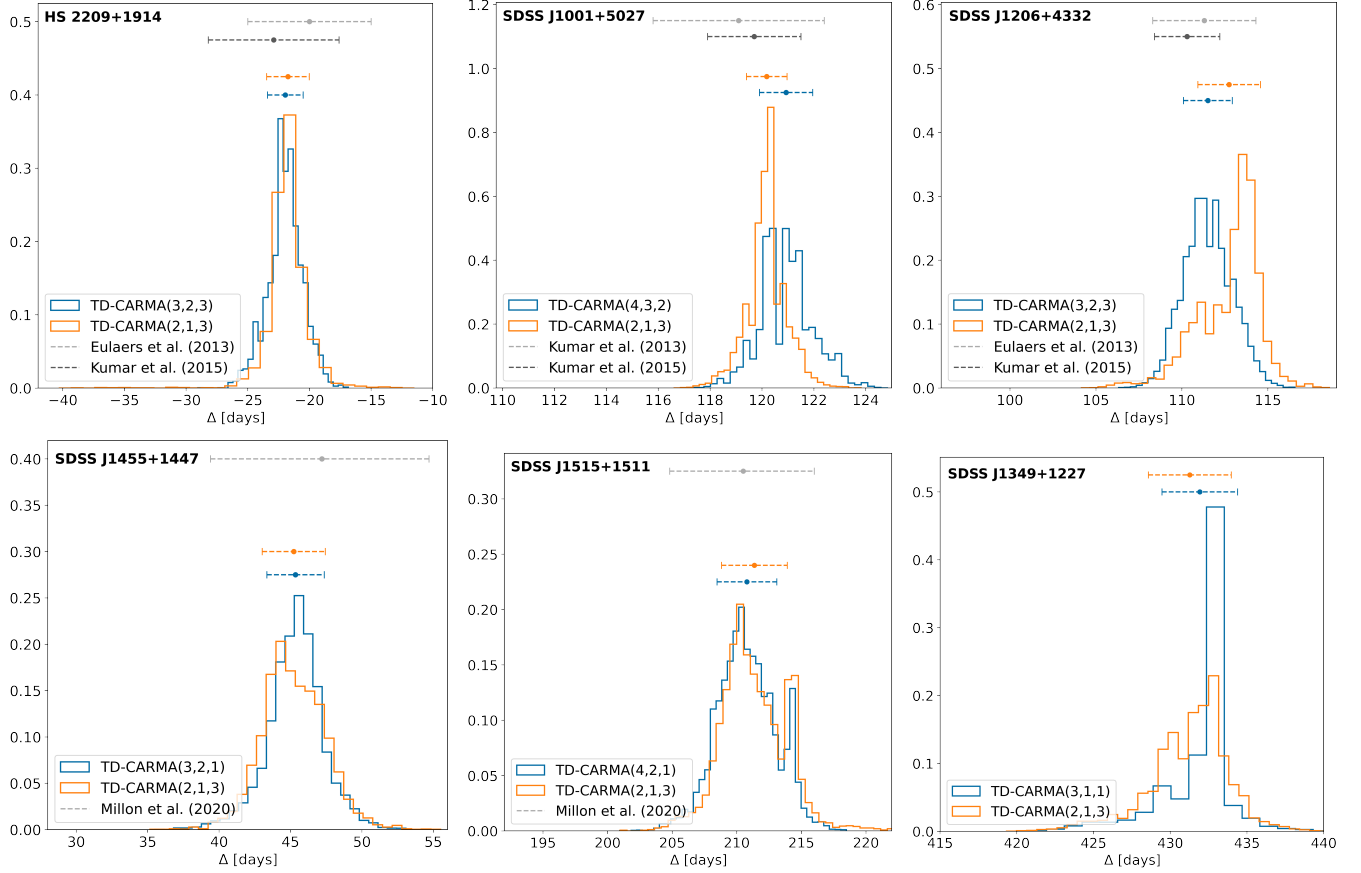


Figure 4. Point estimates and 1σ error bars obtained both by our highest evidence model and the baseline model, i.e., TD-CARMA(2,1,3), compared to previously published methods in [Eulaers et al. \(2013b\)](#), [Kumar et al. \(2013\)](#) from the COSMOGRAIL collaboration, and [Kumar et al. \(2015\)](#). In all six cases, both our simplest and best model obtain significantly tighter error bounds than those published in the above mentioned papers. On the HS 2209+1914 doubly lensed quasar dataset (top left panel), our methods obtain error bars between 71.04 % and 73.15 % smaller than [Eulaers et al. \(2013b\)](#) and [Kumar et al. \(2015\)](#), corresponding to a reduction in the uncertainty by a factor of ≈ 3.5 . For the SDSS J1001+5027 dataset (top middle panel), we achieve error bars between ≈ 1.8 and ≈ 4.4 times smaller than existing analysis, (depending on which model we use and which method we compare it to). For SDSS J1206+4332 (top right panel), we reduce the error estimates by a factor of $\approx 1.12 - 2.06$

days (see Table 11); the latter is consistent with the literature ([Eulaers et al. 2013b](#); [Kumar et al. 2015](#)). (Our fitted $\hat{\Delta}$ for all models that did not detect a frequency appear in Table 11 in Appendix B.) To conduct more principled model comparison when models indicate different possibilities of Δ , we use the values of $\ln(\mathcal{Z})$ computed by MultiNest. This allows us to quantify the evidence in favor of models with $m = 3$, and the posterior probability of each model, via Equation 10. The cumulative probability of the $m = 3$ models is 0.999.

Our implementation of TD-DRW using MultiNest produced a (joint) posterior distributions with a total of 10 modes, and modes for Δ spanning from ≈ -11 days to ≈ 43 days. The bulk of the probability mass of the posterior of Δ under TD-DRW is around ≈ 20 days, which indicates that TD-DRW fails even to get the sign of Δ correct. In addition, Tables 4, 11 and 12 show the

Table 4. Posterior mean and standard deviation for Δ under the models with highest Bayesian log-evidence, with relative probability π summing to 0.999, for HS 2209+1914.

Model	$\hat{\Delta}$	$SD(\hat{\Delta})$	$\ln(\mathcal{Z})$	π
TD-DRW(3)	20.23	0.918	2536.00	0.000
TD-CARMA(3, 2, 3)	-21.96	1.448	2760.24	0.601
TD-CARMA(4, 2, 3)	-21.95	1.403	2759.83	0.399

Bayesian evidence $\ln(\mathcal{Z})$ in favor of the TD-DRW is the lowest of all the considered models.

The top left panel of Figure 4 compares the posterior distributions for Δ under the TD-CARMA model with the highest evidence, i.e., TD-CARMA(3, 2, 3), and the baseline model, i.e., TD-CARMA(2, 1, 3), with esti-

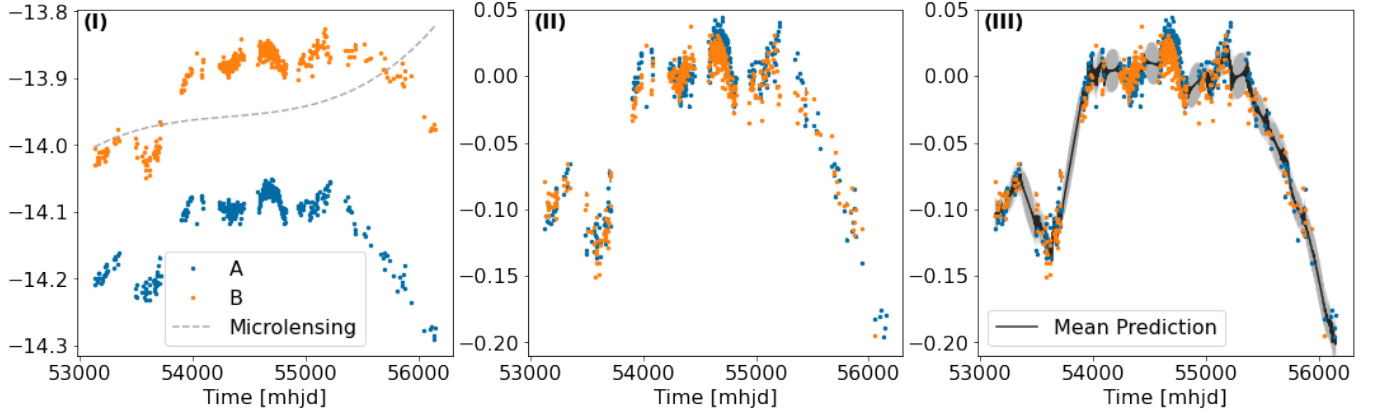


Figure 5. Panel (I) shows the data for the HS2209+1914 doubly lensed quasar, and the microlensing polynomial regression curve (with $m = 3$) fit to lightcurve B (corresponding to measurements \mathbf{y} in our mathematical notation reported in Table 1). The effect of microlensing can be seen, for example in the time period between 55500 and 56000 mhjd, where lightcurve B features a slower decay in magnitude than lightcurve A. This is successfully captured and adjusted for by the increasing behaviour in the fitted microlensing curve. Panel (II) shows the data in Panel (I), adjusted for time delay Δ and the microlensing effect modeled by the polynomial regression, which corresponds to the composite light curve \mathbf{z} defined in Equation 4. Panel (III) shows the mean fitted values (and uncertainties) of the CARMA(3,2) process to composite light curve \mathbf{z} .

Table 5. Comparison of our highest evidence model, i.e., TD-CARMA(3, 2, 3), and our baseline TD-CARMA(2, 1, 3), to estimates of Δ for HS 2209+1914 in the literature.

Technique	$\hat{\Delta}$	$\text{SD}(\hat{\Delta})$
Dispersion ^a	-20.99	10.09
Difference ^a	-20.08	13.78
Spline ^a	-19.77	6.03
NMF ^a	-19.28	1.48
Combination of four above ^a	-20	5
Difference-smoothing (modified) ^b	-22.9	5.3
Running Optimal Average ^c	-24.0	2.4
TD-CARMA(2, 1, 3)	-21.74	1.423
TD-CARMA(3, 2, 3)	-21.96	1.448

^aEulaers et al. (2013b), where estimates for Δ are reported without the minus sign, as they swap labels for the two light curves compared to our notation.

^bKumar et al. (2015).

^cDonnan et al. (2021).

mates found in the astrophysics literature. . Eulaers et al. (2013b) propose an estimate of $\hat{\Delta} = -20 \pm 5$ days, and Kumar et al. (2015) give $\hat{\Delta} = -22.9 \pm 5.3$ days. TD-CARMA(3, 2, 3) and TD-CARMA(2, 1, 3) estimate $\hat{\Delta} = -21.96 \pm 1.448$ and $\hat{\Delta} = -21.74 \pm 1.423$, hence significantly reducing the error bars relative to existing methods (see Table 5). The simulation study in Section 4 demonstrates

Table 6. Posterior mean and standard deviation for Δ under the five models with highest Bayesian log-evidence, for SDSS J1001+5027.

Model	$\hat{\Delta}$	$\text{SD}(\hat{\Delta})$	$\ln(\mathcal{Z})$	π
TD-DRW(3)	132.71	0.770	1803.30	0.000
TD-CARMA(4, 3, 2)	120.93	1.015	2761.25	0.416
TD-CARMA(4, 3, 3)	120.21	1.018	2761.12	0.366
TD-CARMA(3, 2, 3)	120.16	1.003	2759.48	0.104
TD-CARMA(3, 2, 2)	120.88	1.013	2759.44	0.068
TD-CARMA(4, 2, 3)	120.21	0.970	2758.35	0.023

SDSS J1001+5027 is a doubly lensed quasar, observed by the COSMOGRAIL collaboration (Kumar et al. 2013) with three telescopes: Mercator, Maidanak and HCT for more than six years (from March 2005 to July 2011), producing 443 observational epochs.

Our implementation of TD-DRW using MultiNest produced a (joint) posterior distributions with a total of 20 modes, and modes for Δ spanning values from ≈ 123 days and ≈ 135 days. The bulk of the probability mass of the posterior of Δ is around ≈ 132 days, almost two weeks away from the consensus value in the relevant literature, which is ≈ 120 days. The TD-DRW(3) model has $\ln(\mathcal{Z}) = 1803.30$, well below that of any of the TD-CARMA(p, q, m) (see Tables 6 and 13).

Table 6 shows the five TD-CARMA(p, q, m) with the highest Bayesian (log) evidences, as well as their relative probabilities, π_i , computed as detailed in Section 3.3. Together the 5 top models account for 97.7% of the total model probabilities. For given values of hyperpa-

5.3. Application II: SDSS J1001+5027

Table 7. Comparison of our highest evidence model, i.e., TD-CARMA(4, 3, 2), and our baseline, TD-CARMA(2, 1, 3), to estimates of Δ for SDSS J1001+5027 in the literature.

Technique	$\hat{\Delta}$	SD($\hat{\Delta}$)
Dispersion-like ^a	120.5	6.2
Difference-smoothing ^a	118.6	3.7
Regression difference ^a	121.1	3.8
Free-knot spline ^a	119.7	2.6
Combination of four above ^a	119.1	3.3
Gaussian Processes ^b	117.8	3.2
Difference-smoothing (modified) ^c	119.7	1.8
Running Optimal Average ^d	119.9	(-1.5, 1.4)
TD-CARMA(2, 1, 3)	120.18	0.749
TD-CARMA(4, 3, 2)	120.93	1.015

^aEulaers et al. (2013b).

^bHojjati et al. (2013).

^cKumar et al. (2015).

^dDonnan et al. (2021).

rameters p and q , the increase in $\ln(\mathcal{Z})$ obtained from increasing m is small, indicating a weak effect of microlensing in this observation; see Tables 6 and 13 (the latter in Appendix B).

In Table 7, we compare the TD-CARMA(p, q, m) model with the highest Bayesian (log) evidence, i.e., TD-CARMA(4, 3, 2), with recently published analyses of SDSS J1001+5027. TD-CARMA(4, 3, 2) produces error bars that are between 30% and 83.63% lower than existing methods; the baseline model, i.e., TD-CARMA(2, 1, 3), produces error bars that are between 48.34 % and 87.92% lower. The larger error bars of TD-CARMA(4, 3, 2) relative to TD-CARMA(2, 1, 3) may be attributable to a bias-variance trade off: more highly-parameterized models are more flexible and tend to provide better fits, but at the cost of higher levels of uncertainty.

Kumar et al. (2013), the main reference in the estimation of the time delay of SDSS J1001+5027, argue that their four independent measurement techniques (listed in Table 7) each have their own limitations and thus combine the individual estimations from each method to produce their final estimate: $\hat{\Delta} = 119.3 \pm 3.3$ days. Our final estimate is $\hat{\Delta} = 120.93 \pm 1.015$ days, thus providing a consistent (since our posterior distribution covers their estimate) yet novel estimate of the time delay, that is 3 times more certain.

5.4. Application III: SDSS J1206+4332

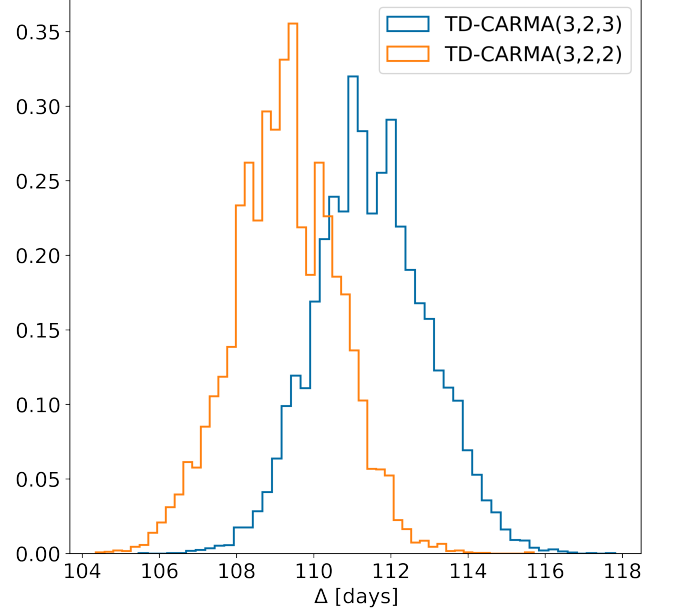


Figure 6. Histograms of posterior draws for Δ under TD-CARMA(3, 2, 2) and TD-CARMA(3, 2, 3), for doubly lensed quasar dataset SDSS J1206+4332.

Table 8. Posterior mean and standard deviation for Δ under the five models with highest Bayesian log-evidence, for SDSS J1206+4332.

Model	$\hat{\Delta}$	SD($\hat{\Delta}$)	$\ln(\mathcal{Z})$	π
TD-DRW(3)	114.68	1.413	1551.02	0.000
TD-CARMA(3, 2, 3)	111.51	1.452	1639.06	0.999
TD-CARMA(3, 2, 2)	109.27	1.351	1628.43	2.42e-5
TD-CARMA(2, 1, 3)	112.78	1.693	1624.65	5.52e-7
TD-CARMA(3, 1, 3)	112.77	1.670	1623.66	2.05e-7
TD-CARMA(2, 1, 2)	108.33	2.240	1616.64	1.83e-10

SDSS J1206+4332 is a doubly lensed quasar observed by the COSMOGRAIL collaboration (Eulaers et al. 2013b) with three telescopes: Maidanak, Mercator and HCT for a total of seven years (from 2005 to 2011).

For this data, TD-DRW has the lowest Bayesian evidence of the set of considered models, and has a relative probability of essentially 0 (up to numerical precision). TD-DRW produces a joint posterior distribution with 6 modes, with posterior modes for Δ ranging from ≈ 106 days to ≈ 117 days. Even though our computational procedure allows us to obtain a sample from the posterior (whereas the MCMC based implementation of TD-DRW in the *timedelay* package from Tak et al. (2017) fails to converge), TD-DRW does not appear to be sufficiently flexible for this data.

Table 9. Comparison of our highest evidence model, i.e., TD-CARMA(3, 2, 3), and our baseline TD-CARMA(2, 1, 3), to estimates of Δ for SDSS J1206+4332 in the literature.

Technique	$\hat{\Delta}$	SD($\hat{\Delta}$)
Dispersion ^a	113.65	6.79
Difference ^a	109.73	8.28
Spline ^a	111.31	3.93
NMF ^a	113.80	0.90
<i>Combination of four above^a</i>	111.3	3
Splines + Regression Difference ^b	111.8	(-2.7, 2.4)
Difference-smoothing (modified) ^c	110.3	1.9
Running Optimal Average ^d	113.0	(-1.2, 1.1)
TD-CARMA(2, 1, 3)	112.78	1.693
TD-CARMA(3, 2, 3)	111.51	1.452

^aEulaers et al. (2013b).

^bBirrer et al. (2019).

^cKumar et al. (2015).

^dDonnan et al. (2021).

Turning to fits obtained with TD-CARMA, Table 8 shows that the posterior distribution of Δ is sensitive to the value of m , which indicates the presence of a strong microlensing effect in this observation. Indeed, Figure 6 illustrates that third order polynomial regression seems to pull the posterior distribution of Δ towards ≈ 112 days, whereas posterior distributions of Δ obtained with $m = 2$ tend to center around ≈ 109 days. The posterior PSDs of the intrinsic light curve under both models are identical, which shows that this effect is indeed solely attributable to microlensing. In some cases, such as TD-CARMA(2, 1, 3), the posterior distribution covers both areas of likely values. This is also the case in Eulaers et al. (2013b), where the Numerical Model Fit (NMF) technique estimates $\hat{\Delta} = 113.80 \pm 0.80$ whereas the Spline technique finds $\hat{\Delta} = 111.31 \pm 3.93$. This suggests that either the observational sampling does not allow a strong constraint for Δ , or that the effect of microlensing may be too complex for the currently employed modeling approaches.

TD-CARMA(3, 2, 3) dominates the model space, with probability 0.999, and estimates $\hat{\Delta} = 111.51 \pm 1.452$ days. This halves the uncertainty of Eulaers et al. (2013b) (111.3 ± 3 days), and reduces the uncertainty derived in Kumar et al. (2015) by 23.58% (110.3 ± 1.9 days), as shown in Table 9. Although the estimate produced by Donnan et al. (2021) (see “Running Optimal Average Method” in Table 9) has less uncertainty than TD-CARMA for this particular data, its similarity to the results obtained by the NMF technique (Eulaers

Table 10. Comparing (posterior) power of the detected frequencies with the measurement noise level.

Dataset	Frequency	99% power ^a	Noise level ^a
J1206	≈ 1 days	[1.69, 2.94]	10.67
J1001	≈ 2 days	[0.22, 0.92]	0.60
HS 2209	≈ 1 days	[1.28, 3.94]	2.29

^aValues are given ($\times 10^{-4}$)

et al. 2013b) suggest that it may have left part of the parameter space unexplored.

5.5. Numerical Evaluation of Frequencies

in Appendix B show that under some of the TD-CARMA(p, q, m), the posterior distribution of the CARMA parameters (α, β, σ) correspond to PSDs with a frequency (i.e., a Lorentzian centered away from 0), either for specific modes or for the whole distribution. For instance, one mode of the posterior PSD under TD-CARMA(3, 1, 1) fitted to the SDSS J1206+4332 data has frequency of ≈ 1 day, and the posterior PSD under TD-CARMA(4, 1, 3) fitted to the SDSS J001+5027 data finds a frequency of ≈ 2 days.

These frequencies might be an inherent property of the intrinsic light curves themselves, or simply a feature of the measurement noise.

Table 10 shows the (posterior mean of the) detected frequencies, the associated 99% posterior intervals for the power, and the measurement noise level. In all three cases, the 99% posterior interval for the power of the detected frequencies either cover or are well below the measurement noise level¹⁰. We therefore discard all models that detect a frequency in our analyses.

6. CONCLUSION

We present TD-CARMA, an extension to TD-DRW presented by Tak et al. (2017) and designed to perform Bayesian estimation of cosmological time delay arising in gravitationally lensed systems of light curves. Because they are more flexible and more widely applicable for modelling the intrinsic stochastic variability of AGN light curves, we employ CARMA processes in our extension and thus design an accurate general method applicable to a wide range of AGN lensed systems.

Our simulation studies and data applications demonstrate that our method is applicable and produces precise time delay estimates on datasets that cannot be

analyzed by the DRW-based method proposed by Tak et al. (2017).

The computational aspects of our method also allow a number of improvements over existing methods. First, the method does not require a user-specified initial value of the time delay parameter Δ . Our MultiNest-based Bayesian inference engine is robust to multimodal posterior distributions, which arise frequently both in CARMA processes and in time delay estimation problems. Finally, our method directly computes the Bayesian evidence for the fitted model. This allows us to perform principled Bayesian model comparison and selection, for instance to select hyperparameters including the order of the CARMA process and microlensing model.

There are several potential improvements and additional applications of TD-CARMA beyond what we present in this work. The models developed in this article only account for single-band light curves. Hu & Tak (2020) developed a method to model multi-band light curves using the DRW process, and show that it yields more precise time delay estimates. An avenue for future research would be to extend our method to multi-band light curves. , we carried out a prior sensitivity analysis and empirically verified the robustness of our model selection procedure to the choice of priors. Although we find that TD-CARMA estimates of Δ and their error bars are not particularly dependent on the choice of priors placed on the intrinsic light curve and microlensing parameters, the Bayesian evidence, \mathcal{Z} , tends to be more sensitive to priors. Thus, the choice of model, based on \mathcal{Z} , can be more prior dependent. Insofar as the ultimate aim is to estimate the time delay, however, this is only a concern if there are competing models with appreciable posterior probability that deliver substantively different estimates of Δ .

Variants of TD-CARMA might also be applied to problems outside of time delay estimation. Time delays also arise in reverberation mapping, where the emission-line response is delayed with respect to changes in the continuum in accretion flows around supermassive black holes. The estimation of this delay can be used to estimate the mass of the black hole.

Software: TD-CARMA: https://github.com/antoinedmeyer/td_carma, MultiNest (Feroz et al. 2009; Buchner 2016), .

The COSMOGRAIL data for the HS 2209+1914, SDSS J1001+5027, SDSS J1206+4332 doubly lensed quasar datasets is publicly available online at https://obswww.unige.ch/~millon/d3cs/COSMOGRAIL_public/code.php.

ACKNOWLEDGEMENTS

This work was conducted under the auspices of the CHASC International Astrostatistics Center. CHASC is supported by NSF grants DMS-18-11308, DMS-18-11083, DMS-18-11661, DMS-21-13615, DMS-21-13397, and DMS-21-13605; by the UK Engineering and Physical Sciences Research Council [EP/W015080/1]; and by NASA 18-APRA18-0019. We thank CHASC members for many helpful discussions, especially Vinay Kashyap and Kaisey Mandel, and we thank Andy Thomas for his continuous help and support on computational matters. ADM is supported by the EPSRC Centre for Doctoral Training in Modern Statistics and Statistical Machine Learning (EP/S023151/1). DvD and ADM were also supported in part by a Marie-Skłodowska-Curie RISE Grant (H2020-MSCA-RISE-2019-873089) provided by the European Commission. AS further acknowledges support from NASA contract to the Chandra X-ray Center NAS8-03060.

REFERENCES

- Abell, P. A., Allison, J., Anderson, S. F., et al. 2009, arXiv preprint arXiv:0912.0201
- Ade, P. A., Aghanim, N., Armitage-Caplan, C., et al. 2014, *Astronomy & Astrophysics*, 571, A16
- Aghamousa, A., & Shafieloo, A. 2014, arXiv preprint arXiv:1410.8122
- Andrae, R., Kim, D.-W., & Bailer-Jones, C. A. 2013, *Astronomy & Astrophysics*, 554, A137
- Bag, S., Kim, A. G., Linder, E. V., & Shafieloo, A. 2021, *The Astrophysical Journal*, 910, 65
- Bag, S., Shafieloo, A., Liao, K., & Treu, T. 2022, *The Astrophysical Journal*, 927, 191
- Birrer, S., Millon, M., Sluse, D., et al. 2022, arXiv e-prints, arXiv:2210.10833. <https://arxiv.org/abs/2210.10833>
- Birrer, S., Treu, T., Rusu, C., et al. 2019, *Monthly Notices of the Royal Astronomical Society*, 484, 4726
- Bonvin, V., Chan, J. H. H., Millon, M., et al. 2018, *Astronomy & Astrophysics*, 616, A183, doi: [10.1051/0004-6361/201833287](https://doi.org/10.1051/0004-6361/201833287)
- Bonvin, V., Courbin, F., Suyu, S. H., et al. 2016, *Monthly Notices of the Royal Astronomical Society*, 465, 4914, doi: [10.1093/mnras/stw3006](https://doi.org/10.1093/mnras/stw3006)
- Bonvin, V., Millon, M., Chan, J. H.-H., et al. 2019, *A&A*, 629, A97, doi: [10.1051/0004-6361/201935921](https://doi.org/10.1051/0004-6361/201935921)

- Brockwell, P. J. 2001, *Annals of the Institute of Statistical Mathematics*, 53, 113
- Brockwell, P. J., & Davis, R. A. 2002, *Introduction to time series and forecasting* (Springer)
- Buchner, J. 2016, *Astrophysics Source Code Library*, ascl
- Courbin, F., Chantry, V., Revaz, Y., et al. 2011, *Astronomy & Astrophysics*, 536, A53
- Courbin, F., Bonvin, V., Buckley-Geer, E., et al. 2018, *A&A*, 609, A71, doi: [10.1051/0004-6361/201731461](https://doi.org/10.1051/0004-6361/201731461)
- Dobler, G., Fassnacht, C. D., Treu, T., et al. 2015, *The Astrophysical Journal*, 799, 168
- Donnan, F. R., Horne, K., & Hernández Santisteban, J. V. 2021, *MNRAS*, 508, 5449, doi: [10.1093/mnras/stab2832](https://doi.org/10.1093/mnras/stab2832)
- Eulaers, E., Tewes, M., Magain, P., et al. 2013a, *A&A*, 553, A121, doi: [10.1051/0004-6361/201321140](https://doi.org/10.1051/0004-6361/201321140)
- Eulaers, E., Tewes, M., Magain, P., et al. 2013b, *Astronomy & Astrophysics*, 553, A121
- Feroz, F., Hobson, M., & Bridges, M. 2009, *Monthly Notices of the Royal Astronomical Society*, 398, 1601
- Gander, W. 1980, *Res. Rep.*, 80, 1251
- Graham, M. J., Djorgovski, S. G., Drake, A. J., et al. 2014, *Monthly Notices of the Royal Astronomical Society*, 439, 703, doi: [10.1093/mnras/stt2499](https://doi.org/10.1093/mnras/stt2499)
- Hojjati, A., Kim, A. G., & Linder, E. V. 2013, *Physical Review D*, 87, 123512
- Hu, Z., & Tak, H. 2020, *The Astronomical Journal*, 160, 265
- Jefferys, W. H., & Berger, J. O. 1991, *Technical Report*, 157
- Jones, R. H. 1981, in *Applied time series analysis II* (Elsevier), 651–682
- Kasliwal, V. P., Vogeley, M. S., & Richards, G. T. 2015, *Monthly Notices of the Royal Astronomical Society*, 451, 4328, doi: [10.1093/mnras/stv1230](https://doi.org/10.1093/mnras/stv1230)
- Kasliwal, V. P., Vogeley, M. S., & Richards, G. T. 2017, *Monthly Notices of the Royal Astronomical Society*, 470, 3027
- Kass, R. E., & Raftery, A. E. 1995, *Journal of the American Statistical Association*, 90, 773
- Kelly, B. C., Bechtold, J., & Siemiginowska, A. 2009, *The Astrophysical Journal*, 698, 895
- Kelly, B. C., Becker, A. C., Sobolewska, M., Siemiginowska, A., & Uttley, P. 2014, *The Astrophysical Journal*, 788, 33
- Kim, D.-W., Protopapas, P., Trichas, M., et al. 2012, *The Astrophysical Journal*, 747, 107
- Kochanek, C., Morgan, N., Falco, E., et al. 2006, *The Astrophysical Journal*, 640, 47
- Kozłowski, S. 2016, *Monthly Notices of the Royal Astronomical Society*, 459, 2787, doi: [10.1093/mnras/stw819](https://doi.org/10.1093/mnras/stw819)
- . 2017, *A&A*, 597, A128, doi: [10.1051/0004-6361/201629890](https://doi.org/10.1051/0004-6361/201629890)
- Kozłowski, S., Kochanek, C. S., Udalski, A., et al. 2009, *The Astrophysical Journal*, 708, 927
- Kumar, S. R., Stalin, C., & Prabhu, T. 2015, *Astronomy & Astrophysics*, 580, A38
- Kumar, S. R., Tewes, M., Stalin, C., et al. 2013, *Astronomy & Astrophysics*, 557, A44
- Liao, K., Treu, T., Marshall, P., et al. 2015, *The Astrophysical Journal*, 800, 11
- Linder, E. V. 2011, *Phys. Rev. D*, 84, 123529, doi: [10.1103/PhysRevD.84.123529](https://doi.org/10.1103/PhysRevD.84.123529)
- MacLeod, C. L., Ivezić, Ž., Kochanek, C., et al. 2010, *The Astrophysical Journal*, 721, 1014
- Millon, M., Courbin, F., Bonvin, V., et al. 2020a, *A&A*, 642, A193, doi: [10.1051/0004-6361/202038698](https://doi.org/10.1051/0004-6361/202038698)
- Millon, M., Courbin, F., Bonvin, V., et al. 2020b, *Astronomy & Astrophysics*, 640, A105
- Moreno, J., Vogeley, M. S., Richards, G. T., & Yu, W. 2019, *Publications of the Astronomical Society of the Pacific*, 131, 063001
- Morgan, C. W., Hainline, L. J., Chen, B., et al. 2012, *The Astrophysical Journal*, 756, 52
- Mushotzky, R. F., Edelson, R., Baumgartner, W., & Gandhi, P. 2011, *The Astrophysical Journal Letter*, 743, L12, doi: [10.1088/2041-8205/743/1/L12](https://doi.org/10.1088/2041-8205/743/1/L12)
- Pelt, J., Hoff, W., Kayser, R., Refsdal, S., & Schramm, T. 1994, *A&A*, 286, 775, <https://arxiv.org/abs/astro-ph/9401013>
- Protassov, R., Van Dyk, D. A., Connors, A., Kashyap, V. L., & Siemiginowska, A. 2002, *The Astrophysical Journal*, 571, 545
- Rathna Kumar, S., Tewes, M., Stalin, C. S., et al. 2013, *A&A*, 557, A44, doi: [10.1051/0004-6361/201322116](https://doi.org/10.1051/0004-6361/201322116)
- Refsdal, S. 1964, *Monthly Notices of the Royal Astronomical Society*, 128, 307
- Ryan, J. L., Siemiginowska, A., Sobolewska, M., & Grindlay, J. 2019, *The Astrophysical Journal*, 885, 12
- Ryan, J. L., Siemiginowska, A., Sobolewska, M. A., & Grindlay, J. 2019, *ApJ*, 885, 12, doi: [10.3847/1538-4357/ab426a](https://doi.org/10.3847/1538-4357/ab426a)
- Shah, P., Lemos, P., & Lahav, O. 2021, *A&A Rv*, 29, 9, doi: [10.1007/s00159-021-00137-4](https://doi.org/10.1007/s00159-021-00137-4)
- Skilling, J. 2006, *Bayesian analysis*, 1, 833
- Stone, Z., Shen, Y., Burke, C. J., et al. 2022, *Monthly Notices of the Royal Astronomical Society*, 514, 164, doi: [10.1093/mnras/stac1259](https://doi.org/10.1093/mnras/stac1259)
- Suyu, S. H., Bonvin, V., Courbin, F., et al. 2017, *Monthly Notices of the Royal Astronomical Society*, 468, 2590, doi: [10.1093/mnras/stx483](https://doi.org/10.1093/mnras/stx483)

- Tak, H., Mandel, K., Van Dyk, D. A., et al. 2017, The Annals of Applied Statistics, 1309
- Tak, H., Meng, X.-L., & van Dyk, D. A. 2018, Journal of Computational and Graphical Statistics, 27, 479
- Tewes, M., Courbin, F., & Meylan, G. 2013, Astronomy & Astrophysics, 553, A120
- Treu, T., & Marshall, P. J. 2016, The Astronomy and Astrophysics Review, 24, 11
- Treu, T., Suyu, S. H., & Marshall, P. J. 2022, arXiv e-prints, arXiv:2210.15794.
<https://arxiv.org/abs/2210.15794>
- Tsai, H., & Chan, K. S. 2000, Statistica Sinica, 10, 989.
<http://www.jstor.org/stable/24306759>
- Tsai, H., Chan, K.-S., & Fayard, P. 2011, Statistics and Its Interface, 4, 235
- Verde, L., Treu, T., & Riess, A. G. 2019, Nature Astronomy, 3, 891, doi: [10.1038/s41550-019-0902-0](https://doi.org/10.1038/s41550-019-0902-0)
- Zu, Y., Kochanek, C. S., Kozłowski, s., & Udalski, A. 2013, The Astrophysical Journal, 765, 106, doi: [10.1088/0004-637X/765/2/106](https://doi.org/10.1088/0004-637X/765/2/106)

APPENDIX

A. MODELLING STOCHASTIC VARIABILITY IN ASTRONOMICAL OBJECTS

To compare different classes of stochastic processes and to gain insight about the underlying process governing their variability, it is useful to inspect the Auto-Covariance Function (ACF) and Power Spectral Density (PSD).

A.1. *The DRW process*

The ACF of a stochastic process $X(t)$, $t \in \mathbb{R}$ is defined as $E[(X(t_i) - E(X(t_i)))(X(t_j) - E(X(t_j)))]$, and gives the covariance of the process with itself at two different times. The ACF of a DRW process is given by:

$$R(d_{ij}) = \frac{\sigma^2 \tau}{2} e^{-\frac{d_{ij}}{\tau}}, \quad (\text{A1})$$

where $d_{ij} = t_i - t_j$ is the time difference between any two observation times t_i and t_j , with $t_i > t_j$ (Kelly et al. 2009). The ACF in Equation A1 features an exponentially decaying component with e -folding timescale τ which highlights the mean-reverting behaviour of the DRW process.

The PSD, defined as the Fourier Transform of the ACF, describes the distribution of power¹¹ over frequencies for continuous and stationary stochastic processes. The PSD of the DRW process, given by:

$$P(f) = \sigma^2 \frac{1}{(\frac{1}{\tau})^2 + (2\pi f)^2}, \quad (\text{A2})$$

is a Lorentzian centered at 0, with a break frequency at $1/2\pi\tau^2$ (Kelly et al. 2009). This illustrates the limited applicability of a DRW process in describing the stochastic variability in light curves. For example, quasi-periodic variability features in an AGN light curve can be represented as Lorentzians centered away from 0, hence a DRW process would be unable to characterize this type of variability. Moreover, the DRW process can only account for a single break frequency in the PSD, which renders it somewhat inflexible.

A.2. *The CARMA processes*

To ensure stationarity of the process, we must have $q < p$, and the roots of the auto-regressive polynomial $A(z)$, defined as:

$$A(z) = \sum_{k=0}^p \alpha_k z^k, \quad (\text{A3})$$

¹¹ The power of a stochastic process is defined as the squared value of the process, i.e., the power of process $X(t)$ is given by $|X(t)|^2$.

must have negative real parts (Kelly et al. 2014; Tsai & Chan 2000; Tsai et al. 2011). In practice, this constraint is more easily enforced when considering an alternative parametrization of the auto-regressive polynomial (Jones 1981; Kelly et al. 2014), obtained by factorizing it into linear and quadratic terms as follows:

$$A(z) = (a_1 + a_2 z + z^2)(a_3 + a_4 z + z^2) \dots \times \begin{cases} a_{p-1} + a_p z + z^2 & \text{if } p \text{ is even,} \\ a_p + z & \text{if } p \text{ is odd.} \end{cases}$$

The roots of the auto-regressive polynomial are negative if the coefficients $\mathbf{a} = \{a_1 \dots, a_p\}$ are positive. We discuss computational strategies for stable implementation and inference in Section 3.4.

The PSD of a stationary CARMA(p , q) process is given by:

$$P(f) = \sigma^2 \frac{|\sum_{j=0}^q \beta_j (2\pi i f)^j|^2}{|\sum_{k=0}^p \alpha_k (2\pi i f)^k|^2}, \quad (\text{A4})$$

and its ACF is:

$$R(d_{ij}) = \sigma^2 \sum_{k=1}^p \frac{[\sum_{l=0}^q \beta_l r_k^l] [\sum_{l=0}^q \beta_l (-r_k)^l] \exp(r_k d_{ij})}{-2\text{Re}(r_k) \prod_{l=1, l \neq k}^p (r_l - r_k)(r_l^* + r_k)}, \quad (\text{A5})$$

where r_k , $k = 1, \dots, p$ are the roots of the auto-regressive polynomial $A(z)$ (Tsai & Chan 2000; Tsai et al. 2011; Kelly et al. 2014).

The ACF of a CARMA process is therefore a weighted sum of exponentially damped sinusoidal functions (corresponding to complex roots) and exponential decays (corresponding to real roots) (Kelly et al. 2014). A CARMA process has the flexibility to model exponentially decaying auto-correlations with multiple time scales (rather than a single one for the DRW process), and to incorporate periodic oscillations in the auto-correlations. Figure 7 illustrates the difference between DRW and CARMA processes in terms of their auto-correlations and highlights the fact that even within a CARMA(p , q) family, CARMA processes with different orders of p and q may look quite different. This implies that the flexibility of CARMA processes makes them suitable to characterize the variability in a wide range of AGN light curves.

B. DATASET APPLICATION RESULTS

This section reports the summary statistics for TD-DRW and TD-CARMA fitted to the doubly

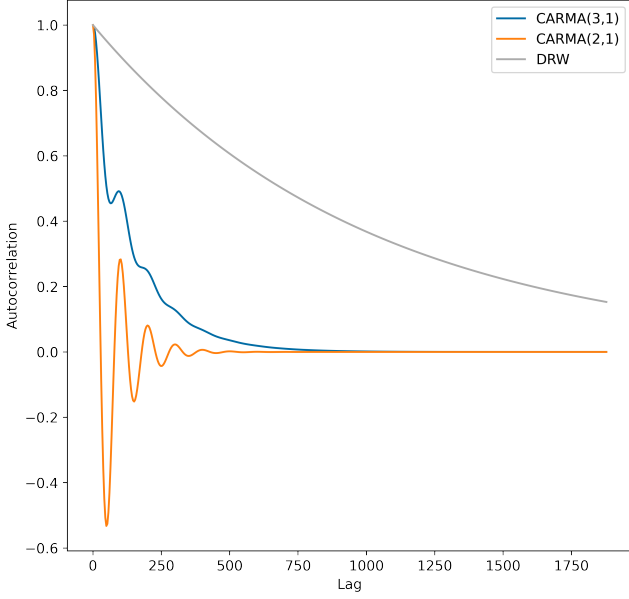


Figure 7. Autocorrelation functions for intrinsic light curve models used in Simulation I.

Table 11. Summary statistics for the models and posterior modes that do not detect a frequency in the (posterior) PSD of the intrinsic light curve model for the HS 2209+1914 doubly lensed quasar.

(p,q,m)	M/n	$\ln(\mathcal{Z})$	$\hat{\Delta}$	$SD(\hat{\Delta})$
(2,1,1)	1/1	2714.62	-42.32	2.430
(2,1,2)	1/1	2723.52	-41.82	2.561
(2,1,3)	1/1	2752.52	-21.74	1.423
(3,1,1)	1/2	2714.37	-43.03	1.952
(3,1,2)	3/3	2723.00	-42.09	2.741
(3,1,3)	1/2	2751.56	-21.73	1.436
(3,2,1)	1/1	2719.65	-38.16	3.324
(3,2,2)	1/1	2729.66	-37.21	3.466
(3,2,3)	1/2	2759.78	-21.96	1.420
(3,2,3)	2/2	2759.23	-21.94	1.460
(4,2,3)	1/3	2759.83	-21.95	1.403
(4,3,2)	1/1	2730.02	-38.17	3.198

NOTE—The "M/n" column denotes the number of the reported mode as given by MultiNest, as well as the total number of modes in the posterior distribution.

lensed quasar datasets HS 2209+1914 (Tables 11 and 12), SDSS J1001+5027 (Tables 13 and 14), SDSS J1206+4332 (Tables 15 and 16), SDSS J1515+1511 (Tables 17 and 18), SDSS J1455+1447 (Tables 19 and 20) and SDSS J1349+1227 (Tables 21 and 22).

Table 12. Same as Table 11 for HS 2209+1914, but for models and posterior modes that detect a frequency, the posterior mean of which is denoted by \hat{f} .

(p,q,m)	M/n	$\ln(\mathcal{Z})$	$\hat{\Delta}$	$SD(\hat{\Delta})$	\hat{f}
(3,1,1)	1/2	2798.63	-36.69	4.029	1.003
(3,1,2)	1/3	2799.77	-36.78	0.791	1.003
(3,1,2)	2/3	2797.64	-44.59	0.428	1.002
(3,1,3)	1/2	2799.68	-32.95	4.672	1.002
(4,1,1)	1/2	2804.15	-29.02	4.672	1.003
(4,1,1)	2/2	2804.08	-28.93	5.184	1.003
(4,1,2)	1/2	2804.18	-34.85	6.110	1.003
(4,1,2)	2/2	2803.72	-35.82	6.795	1.003
(4,1,3)	1/3	2802.87	-27.12	3.335	1.003
(4,1,3)	2/3	2801.53	-26.50	2.917	1.003
(4,1,3)	3/3	2811.39	-28.48	3.728	1.003
(4,2,1)	1/2	2800.93	-25.55	0.431	1.003
(4,2,1)	2/2	2800.25	-30.56	0.384	1.003
(4,2,2)	1/2	2803.36	-34.64	6.367	1.003
(4,2,2)	2/2	2800.34	-36.23	6.249	1.003
(4,2,3)	2/3	2792.02	-25.22	1.993	1.003
(4,2,1)	3/3	2796.89	-29.71	3.243	1.003
(4,3,1)	1/2	2802.54	-35.48	2.254	1.003
(4,3,1)	2/2	2800.97	-34.31	1.724	1.003
(4,3,3)	1/1	2807.15	-28.75	4.521	1.003

NOTE—The posterior mean of the detected frequency is denoted by \hat{f} .

Table 13. Same as Table 11, but for the SDSS J1001+5027 doubly lensed quasar dataset and models and posterior modes that do not detect a frequency.

(p,q,m)	M/n	$\ln(\mathcal{Z})$	$\hat{\Delta}$	$SD(\hat{\Delta})$
(2,1,1)	1/1	2740.09	119.94	0.875
(2,1,2)	1/1	2743.91	120.70	0.799
(2,1,3)	1/1	2744.05	120.18	0.749
(3,1,1)	1/2	2739.26	120.05	0.797
(3,1,2)	1/2	2743.17	120.66	0.753
(3,1,3)	1/2	2743.06	120.23	0.686
(3,2,1)	1/2	2754.78	120.16	1.076
(3,2,1)	2/2	2753.80	119.87	1.117
(3,2,2)	1/1	2759.44	120.88	1.013
(3,2,3)	1/2	2759.48	120.16	1.003
(3,2,3)	2/2	2759.48	120.16	1.040
(4,2,1)	1/1	2753.89	119.94	1.025
(4,2,2)	1/1	2758.21	120.85	0.939
(4,2,3)	1/1	2758.35	120.21	0.970
(4,3,1)	1/1	2756.21	119.85	1.041
(4,3,2)	1/1	2761.25	120.93	1.015
(4,3,3)	1/1	2761.12	120.21	1.018

Table 14. Same as Table 11, but for the SDSS J1001+5027 doubly lensed quasar dataset and models and posterior modes that detect a frequency.

(p,q,m)	M/n	$\ln(\mathcal{Z})$	$\hat{\Delta}$	$SD(\hat{\Delta})$	\hat{f}
(3,1,1)	2/2	2750.12	120.36	0.134	2.00
(3,1,2)	2/2	2743.17	120.42	0.217	2.00
(3,1,3)	1/2	2751.63	120.36	0.224	2.00
(4,1,1)	1/2	2748.84	120.37	0.112	2.00
(4,1,1)	2/2	2748.96	120.36	0.114	2.00
(4,1,2)	1/3	2750.95	120.38	0.018	2.00
(4,1,2)	2/3	2747.68	120.88	0.010	2.00
(4,1,2)	3/3	2750.97	120.41	0.177	2.00
(4,1,3)	1/2	2751.07	120.36	0.187	2.00
(4,1,3)	2/2	2750.92	120.36	0.170	2.00

Table 15. Same as Table 11, but for the SDSS J1206+4332 doubly lensed quasar dataset and models and posterior modes that do not detect a frequency.

(p,q,m)	M/n	$\ln(\mathcal{Z})$	$\hat{\Delta}$	$SD(\hat{\Delta})$
(2,1,1)	1/1	1562.55	112.50	1.454
(2,1,2)	1/1	1616.64	108.33	2.240
(2,1,3)	1/1	1624.65	112.78	1.693
(3,1,1)	2/2	1560.95	112.72	1.379
(3,1,2)	2/2	1613.46	108.44	2.259
(3,1,3)	2/2	1623.66	112.77	1.670
(3,2,1)	1/3	1573.20	112.79	1.288
(3,2,2)	1/2	1628.09	109.27	1.285
(3,2,2)	2/2	1627.21	109.27	1.382
(3,2,3)	1/2	1638.76	111.50	1.389
(3,2,3)	2/2	1637.71	111.50	1.469
(4,2,1)	1/3	1572.10	112.79	1.400

Table 16. Same as Table 11, but for the SDSS J1206+4332 doubly lensed quasar dataset and models and posterior modes that detect a frequency, the posterior mean of which is denoted by \hat{f} .

(p,q,m)	M/n	$\ln(\mathcal{Z})$	$\hat{\Delta}$	$SD(\hat{\Delta})$	\hat{f}
(3,1,1)	1/2	1641.00	107.14	2.332	1.000
(3,1,2)	1/2	1666.11	110.65	0.970	1.000
(3,1,3)	1/2	1667.05	111.07	0.974	1.000
(3,2,1)	2/3	1629.86	109.71	1.255	1.000
(3,2,1)	3/3	1572.42	112.79	1.628	1.000
(4,1,1)	1/2	1641.07	107.63	2.459	1.000
(4,1,1)	2/2	1641.08	107.66	2.428	1.000
(4,1,2)	1/2	1671.95	110.64	0.934	1.000
(4,1,2)	2/2	1665.42	110.60	1.039	1.000
(4,1,3)	1/2	1666.43	111.11	0.965	1.000
(4,1,3)	2/2	1672.39	111.23	0.875	1.000
(4,2,1)	2/3	1635.27	109.18	0.0207	1.000
(4,2,1)	3/3	1634.54	108.20	0.0196	1.000
(4,2,2)	1/3	1669.24	111.06	0.0230	1.000
(4,2,2)	2/3	1668.09	110.06	0.0201	1.000
(4,2,2)	3/3	1663.48	110.72	0.871	1.000
(4,2,3)	1/2	1666.03	111.15	0.969	1.000
(4,2,3)	2/2	1674.30	111.25	0.844	1.000
(4,3,1)	1/2	1643.52	108.43	1.766	1.000
(4,3,1)	2/2	1637.00	108.10	1.346	1.000
(4,3,2)	1/2	1649.08	106.11	0.865	1.000
(4,3,2)	2/2	1671.06	110.66	0.752	1.000
(4,3,3)	1/2	1673.05	111.25	0.713	1.000
(4,3,3)	2/2	1671.18	111.22	0.722	1.000

Table 17. Same as Table 11, but for the SDSS J1515+1511 doubly lensed quasar dataset and models and posterior modes that do not detect a frequency.

(p,q,m)	M/n	$\ln(\mathcal{Z})$	$\hat{\Delta}$	$SD(\hat{\Delta})$
(2,1,1)	1/1	1262.81	211.22	1.953
(2,1,2)	1/2	983.69	-244.07	0.559
(2,1,2)	2/2	1257.34	211.23	2.184
(2,1,3)	1/2	1249.84	211.21	2.108
(2,1,3)	2/2	1004.07	-292.94	2.360
(3,1,1)	1/1	1263.43	211.37	2.013
(3,1,2)	1/5	985.79	-243.97	0.370
(3,1,2)	4/5	1252.47	210.87	1.591
(3,1,2)	5/5	1257.45	211.32	2.165
(3,1,3)	1/3	1004.57	-292.85	2.234
(3,1,3)	3/3	1251.68	211.40	2.165
(3,2,1)	1/1	1274.76	210.66	2.131
(3,2,2)	1/2	1268.86	210.61	2.452
(3,2,2)	1/2	1021.76	-251.84	2.507
(3,2,3)	1/2	1031.68	-250.56	2.487
(3,2,3)	2/2	1263.12	210.72	2.476
(4,2,1)	1/1	1275.44	210.80	2.179
(4,2,2)	1/2	1023.55	-251.82	2.210
(4,2,2)	2/2	1269.33	210.69	2.432
(4,2,3)	1/2	1263.33	210.80	2.492
(4,2,3)	2/2	1032.84	-250.28	2.226
(4,3,2)	1/2	1270.09	210.60	2.393
(4,3,2)	2/2	1021.88	-251.98	2.526
(4,3,3)	1/2	1032.56	-250.79	2.465
(4,3,3)	2/2	1264.36	210.67	2.437

NOTE—The "M/n" column denotes the number of the reported mode as given by MultiNest, as well the total number of modes in the posterior distribution.

Table 18. Same as Table 11, but for the SDSS J1515+1511 doubly lensed quasar dataset and models and posterior modes that detect a frequency, the posterior mean of which is denoted by \hat{f} .

(p,q,m)	M/n	$\ln(\mathcal{Z})$	$\hat{\Delta}$	$SD(\hat{\Delta})$	\hat{f}
(3,1,2)	2/5	1258.89	211.32	2.017	0.672
(3,1,2)	3/5	1262.72	211.46	2.192	2.002
(3,1,3)	2/3	1257.18	211.43	2.236	1.979
(4,1,1)	1/2	1273.04	210.71	1.636	1.994
(4,1,1)	2/2	1273.64	210.74	1.696	1.996
(4,1,2)	1/4	1159.61	-254.00	2.951	1.002
(4,1,2)	2/4	1155.10	-258.14	1.153	1.003
(4,1,2)	3/4	1266.85	210.90	2.287	1.005
(4,1,2)	4/4	1268.53	210.84	1.972	1.977
(4,1,3)	1/4	1185.33	-210.86	16.421	1.002
(4,1,3)	2/4	1184.57	-217.25	24.146	1.002
(4,1,3)	3/4	1262.77	210.93	2.061	1.794
(4,1,3)	4/4	1262.84	210.98	2.101	1.861

NOTE—The "M/n" column denotes the number of the reported mode as given by MultiNest, as well the total number of modes in the posterior distribution.

Table 19. Same as Table 11, but for the SDSS J1455+1447 doubly lensed quasar dataset and models and posterior modes that do not detect a frequency.

(p,q,m)	M/n	$\ln(\mathcal{Z})$	$\hat{\Delta}$	$SD(\hat{\Delta})$
(2,1,1)	1/1	552.04	45.37	1.874
(2,1,2)	1/1	550.46	45.21	1.915
(2,1,3)	1/2	543.10	45.21	1.942
(2,1,3)	2/2	516.24	-146.13	5.964
(3,1,1)	2/2	552.44	45.58	1.878
(3,1,2)	3/3	550.54	45.19	1.877
(3,1,3)	2/4	513.82	173.21	3.473
(3,1,3)	3/4	516.60	-145.73	5.159
(3,2,1)	1/1	552.72	45.36	1.927
(3,2,2)	1/1	550.99	45.28	1.917
(3,2,3)	1/3	516.36	-145.66	2.903
(3,2,3)	3/3	543.70	45.22	1.970
(4,3,3)	1/1	544.43	45.28	1.981

NOTE—The "M/n" column denotes the number of the reported mode as given by MultiNest, as well the total number of modes in the posterior distribution.

Table 20. Same as Table 11, but for the SDSS J1455+1447 doubly lensed quasar dataset and models and posterior modes that detect a frequency, the posterior mean of which is denoted by \hat{f} .

(p,q,m)	M/n	$\ln(\mathcal{Z})$	$\hat{\Delta}$	$SD(\hat{\Delta})$	\hat{f}
(3,1,1)	1/2	551.13	45.49	1.763	2.005
(3,1,2)	1/3	547.88	44.94	1.055	0.485
(3,1,2)	2/3	549.17	45.57	0.945	2.569
(3,1,3)	1/4	514.36	173.39	3.653	1.388
(3,1,3)	4/4	516.52	-145.15	4.635	1.440
(3,2,3)	2/3	517.43	-144.12	4.422	0.112
(4,1,1)	1/3	551.62	45.79	1.334	1.708
(4,1,1)	2/3	551.49	45.79	1.325	1.578
(4,1,1)	3/3	510.95	-136.32	10.961	1.984
(4,1,2)	1/5	519.55	34.71	1.034	1.024
(4,1,2)	2/5	523.01	45.01	1.480	0.990
(4,1,2)	3/5	511.23	-94.78	11.932	1.001
(4,1,2)	4/5	549.05	45.08	1.013	2.176
(4,1,2)	5/5	549.10	45.14	1.138	1.800
(4,1,3)	1/4	517.62	-146.65	4.359	0.225
(4,1,3)	2/4	518.42	-147.05	4.290	0.149
(4,1,3)	3/4	516.11	172.09	3.744	0.123
(4,1,3)	4/4	516.22	172.01	3.812	0.130
(4,2,1)	1/2	552.74	45.94	0.844	1.189
(4,2,1)	2/2	552.70	45.74	0.869	1.141
(4,2,2)	1/2	550.59	45.31	0.966	1.332
(4,2,2)	2/2	550.73	45.30	0.868	1.247
(4,2,3)	1/4	519.05	-142.77	3.730	0.111
(4,2,3)	2/4	519.35	-144.63	4.535	0.113
(4,2,3)	3/4	517.11	172.38	3.883	0.111
(4,2,3)	4/4	517.01	172.15	3.701	0.114
(4,3,1)	1/2	552.40	46.51	0.733	0.115
(4,3,1)	1/2	552.74	46.54	0.703	0.116
(4,3,2)	1/2	550.81	46.14	0.956	0.134
(4,3,2)	2/2	550.88	46.06	1.120	0.139

NOTE—The "M/n" column denotes the number of the reported mode as given by MultiNest, as well the total number of modes in the posterior distribution.

Table 21. Same as Table 11, but for the SDSS J1349+1227 doubly lensed quasar dataset and models and posterior modes that do not detect a frequency.

(p,q,m)	M/n	$\ln(\mathcal{Z})$	$\hat{\Delta}$	$SD(\hat{\Delta})$
(2,1,1)	1/2	697.27	431.17	2.647
(2,1,1)	2/2	663.17	-188.23	2.704
(2,1,2)	1/2	691.76	431.13	2.660
(2,1,2)	2/2	657.66	-185.51	2.852
(2,1,3)	1/2	689.77	431.31	2.399
(2,1,3)	2/2	654.09	-185.82	3.153
(3,1,1)	1/3	663.57	-187.96	2.576
(3,1,1)	2/3	698.77	432.05	1.950
(3,1,2)	1/5	659.95	-185.86	0.855
(3,1,2)	4/5	692.64	431.86	2.193
(3,1,3)	2/4	690.45	432.02	1.154
(3,1,3)	4/4	654.21	-185.99	0.768
(3,2,1)	1/1	698.58	431.09	2.698
(3,2,2)	1/1	692.84	430.82	2.873
(3,2,3)	1/1	691.13	431.11	2.483
(4,1,2)	3/3	693.32	432.12	2.040
(4,1,3)	1/3	690.75	431.82	2.059
(4,2,1)	1/1	698.84	431.65	2.339
(4,2,2)	1/1	693.52	431.33	2.570
(4,2,3)	1/1	691.53	431.34	2.403
(4,3,1)	1/1	698.72	431.42	2.506
(4,3,2)	1/1	693.22	431.15	2.676
(4,3,3)	1/1	691.52	431.32	2.307

NOTE—The "M/n" column denotes the number of the reported mode as given by MultiNest, as well the total number of modes in the posterior distribution.

Table 22. Same as Table 11, but for the SDSS J1349+1227 doubly lensed quasar dataset and models and posterior modes that detect a frequency, the posterior mean of which is denoted by \hat{f} .

(p,q,m)	M/n	$\ln(\mathcal{Z})$	$\hat{\Delta}$	$\text{SD}(\hat{\Delta})$	\hat{f}
(3,1,1)	3/3	698.23	432.31	1.783	0.857
(3,1,2)	2/5	658.59	-186.37	0.403	0.112
(3,1,2)	2/5	662.03	-181.27	6.219	1.007
(3,1,2)	5/5	692.26	432.06	2.144	0.986
(3,1,3)	1/4	690.09	431.88	1.453	1.429
(3,1,3)	3/4	655.05	-185.98	1.907	2.507
(4,1,1)	1/4	698.35	432.75	0.187	0.531
(4,1,1)	2/4	698.30	432.75	0.261	0.550
(4,1,1)	3/4	663.79	-188.88	2.066	2.036
(4,1,1)	4/4	664.05	-182.07	7.044	1.074
(4,1,2)	1/3	692.63	432.78	0.361	0.561
(4,1,2)	2/3	692.71	432.76	0.375	0.561
(4,1,3)	2/3	664.59	-236.90	22.062	1.003
(4,1,3)	3/3	661.61	-232.48	43.940	1.004

NOTE—The "M/n" column denotes the number of the reported mode as given by MultiNest, as well the total number of modes in the posterior distribution.